Eindhoven University of Technology

MASTER

A study on the properties of droplets in dense emulsion simulations

van Woensel, Jean-Paul

Award date:
2021

Link to publication

Technische Universiteit
Eindhoven
University of Technology

Department of Applied Physics

A study on the properties of droplets in dense emulsion simulations

Master Thesis

Jean-Paul van Woensel

Supervisors:
Prof.dr. F. (Federico) Toschi

Committee members:
Prof.dr. F. (Federico) Toschi
Prof.dr. L.P.J. (Leon) Kamp
Prof.dr. J.G.M. (Hans) Kuerten

R-2087-A

Final version

Eindhoven, August 2021

Abstract

The chaotic dynamics of stabilized dense emulsions are challenging due to the complexity of the physics involved that tightly couples microscopic and macroscopic dynamics. While exploring emulsion phenomenology experimentally is rather difficult, mostly due to their opacity, fully resolved numerical simulations provide today a valuable tool to acquire basic fundamental information at individual droplet level. As a matter of fact, there is still much to be understand on the flow of dense binary emulsions. The aim of this thesis is to study the properties of stabilised emulsions via fully resolved direct numerical simulations modelled via a the multi-component Lattice Boltzmann method. The results of this thesis may contribute towards a better understanding of complex dense emulsion flows. In order to study the details of the microscopic dynamics in dense emulsions, we first introduce an algorithm to accurately track individual droplets in the dispersed phase. This tracking algorithm allows to further analyze the trajectories of single or multiple droplets. In particular, we discuss single droplet statistics such as velocity and acceleration PDFs, absolute and relative dispersion and the droplet (velocity) Lagrangian structure function. Finally, we discuss how to employ droplet trajectories to reconstruct information on the underlying gradients of the velocity field.

Keywords: Dense Emulsions, Droplet Tracking, Lattice Boltzmann

Acknowledgements

First of all, I would like to thank Federico Toschi for his support over the past two years. I am grateful for his patience and guidance especially over the past few months writing this thesis. I also want to thank Ivan Girotto, whose PhD thesis provided most of the groundwork this work is based on and always being willing to help.

I am grateful to Leon Kamp and Hans Kuerten for joining the examination committee.

And finally, I want to say thank you to my family and friends. Without their support, I would never have been where I am now.

Contents

Chapter 1

Introduction

Binary emulsions frequently appear in daily life, in industrial processes and in the food industry, for example surrounding dairy products such as milk and mayonnaise [1], but also in enhanced oil production [2] and chemical engineering [3]. Despite how common emulsions are, many aspects of their physics are not yet well understood. This is especially true for dense emulsions, for which the dispersed phase, i.e. the droplets in the emulsion, takes up more than half of the total volume.

In this thesis, simulations on a dense binary emulsion undergoing chaotic laminar flow are analysed by tracking the dispersed phase as individual droplets in time.

The physics of this type of flows is rich and complex, exhibiting effects from small scales dominated by viscosity and surface tension to the large scale dominated by inertia. The importance of these different effects depends on many factors, such as the relative concentration of the components that make up the emulsion, the applied stirring force and the properties of the fluids themselves. Because of this complexity, it is difficult to experimentally study these kinds of flow and, in particular, it is challenging to track the individual droplets in an emulsion.

1.1 Research goals

The aim of this research is twofold:

- we aim at developing an effective droplet tracking algorithm to study dense emulsions;

- we aim at using this algorithm to gain insights into the physical behaviour of droplets in dense emulsions.

Simulations such as the ones used in this thesis can aid in the improving the fundamental understanding of these flows. In particular, the fully resolved simulations provided by the 3D Lattice Boltzmann code (LBE3D) that will be used allows us, in principle, to study the creation, breakup and coalescence of droplets in the dispersed phase of dense emulsions. The raw data from these simulations is also well suited for applying to a tracking algorithm, which will form the focus of this thesis. This is because these simulations are highly optimised [4], giving us access to large amounts of data from relatively long running simulations with different parameters after relatively short CPU time per simulation. A visual example of what these simulations look like is given in Figure 1.1.

These simulations allow us to study the flow field for varying volume fractions and stirring forces, two of the parameters that can be freely chosen. These analyses will be done by only considering the dispersed phase, i.e. the droplets in an emulsion, as opposed to measuring the Eulerian velocity field at each individual point in space. By using appropriate statistics obtained
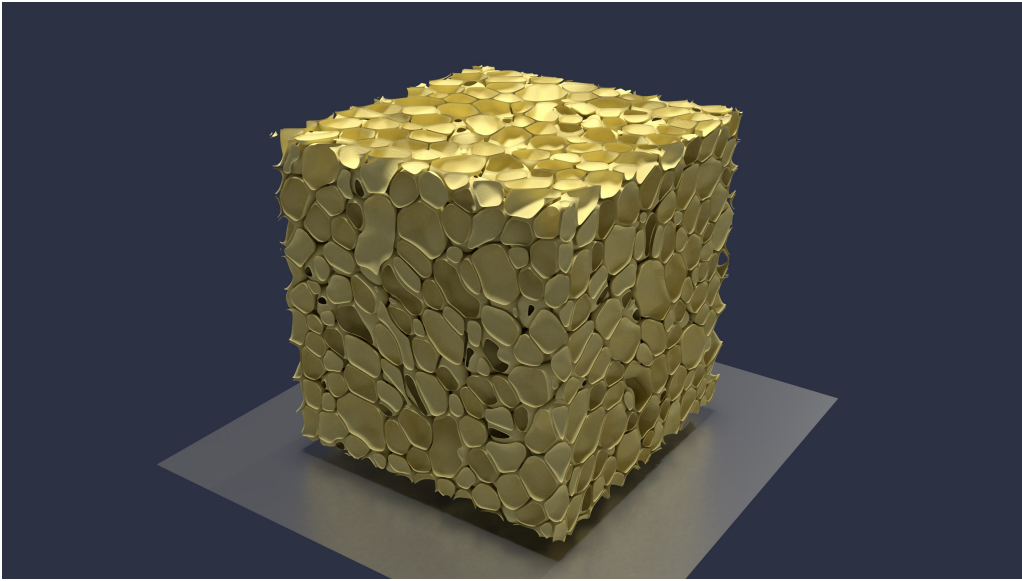
Figure 1.1: Example of a dense emulsion produced by the LBE3D simulations at a high volume fraction of 77%. For clarity, only the dispersed phase is made visible here. Figure adapted from the work of I. Girotto [4]. The full video from which this snapshot was taken can be accessed online [5].

from the individual droplets, we can describe the flow field even without directly measuring the continuous phase.

1.2 Thesis outline

The outline of this thesis is as follows. In chapter 2, we discuss the basic physics necessary to understand what is laid out in this thesis. The physics discussed there cannot, however, be directly applied to a numerical simulation. Therefore, the methodology used to model real world physics through fluid simulations is explained in chapter 3. At the end of the chapter, the method for building up the dense emulsions to be studied is explained. Chapter 4 explains the tracking algorithm that was developed to study the aforementioned simulations. The algorithm is then applied to the simulations, the resulting data of which is analysed in Chapter 5, followed by the conclusions we can draw from our findings.

Chapter 2

The physics of dense emulsions

The motion of fluids is typically described via continuous fields, as their internal structure allows molecules that make up a fluid to have a large freedom in their movement. Indeed, contrary to solids, there is no rigid structure prohibiting the movement of individual molecules with respect to one another, allowing for fluids to flow. In this chapter, the relevant fluid mechanics will be briefly introduced to provide a reference frame for the reader and to establish the notations and conventions that will be used. More specifically, we provide of an overview of the physics relevant to the phenomenology of dense emulsions alongside resources for further reading. There is a focus on the liquid-liquid interfaces that occur at the boundaries of fluid between the two phases of an emulsion.

2.1   Navier-Stokes equations

Different kinds of fluids behave differently when forces are applied to them. In order to derive the velocity field of a fluid, the Navier-Stokes equations can be used, but these equations are not generally applicable due to the assumptions required to derive them. Before we explain the equations themselves, it is therefore necessary to understand these assumptions. We will start by considering how fluids can deform, as the way fluids deform differs based on the characteristics of the particular fluid.

Forces that act on the surface of an object that are aligned parallel to the surface of the object are called shearing forces. This idea can also be applied to fluid parcels, rather than solid objects. The question, then, is how strongly a shearing force causes a fluid parcel to deform. The ratio of shear stress and the rate of shear strain is called the dynamic viscosity μ:

$$\mu = \frac{\text{shear stress}}{\text{shear strain}}. \tag{2.1}$$

In simpler terms, μ is the ratio of the applied shearing force to the deformation of a fluid parcel. The higher the viscosity, the lower the distance the liquid parcel will deform due to an applied shearing force. Honey and syrup are examples of fluids with a high viscosity compared to water, with the former both having a viscosity of the order of 10^3 mPa $\cdot$ s [6] and the latter having a viscosity of 1.002 mPa $\cdot$ s [7] at room temperature.

In the ideal case where the viscosity stays constant, regardless of the strength of the applied forcing, the fluid is referred to as a Newtonian fluid. While no fluid is completely Newtonian, many common fluids such as air and water very closely match the linear relationship between shear stress and the rate of shear strain, making the simple Newtonian model a useful and powerful approximation. We will immediately make use of this, as the Navier-Stokes equations are only valid for Newtonian fluids.

A similar observation can be made for the normal stresses on a fluid parcel, i.e. forces that act perpendicularly to a surface as opposed to parallel to a surface, though the derivation for this is more difficult to express in terms of μ [8].

Now that both shear stresses and normal stresses have been covered, we can move on to the mathematical expressions of the Navier-Stokes equations. They are essentially expressions of Newton's second law in all three spatial dimensions. These equations alone do not suffice to allow for the full flow behaviour to be described analytically, however, due to the non-linear behaviour described by them. For each Cartesian coordinate of the velocity, the Navier-Stokes equations are given by

$$\rho \frac{Dv_i}{Dt} = \rho g_i - \frac{\partial P}{\partial x_i} - \frac{\partial}{\partial x_i}\left(\frac{2}{3}\mu\boldsymbol{\nabla}\cdot\mathbf{v} + \boldsymbol{\nabla}\cdot\left(\mu\frac{\partial\mathbf{v}}{\partial x_i}\right) + \boldsymbol{\nabla}\cdot(\mu\nabla v_i)\right) + F_{ext} \tag{2.2}$$

where $i = x$, y or z.

These equations are valid for both compressible and incompressible flows. The systems that we will consider are deemed to be incompressible, as the density in each fluid component stays nearly constant and the velocities are relatively low (i.e., the Mach number is much smaller than unity). As such, the divergence is zero, i.e. $\nabla\cdot\mathbf{v} = 0$. Additionally, gravity is not considered in the simulations, so the above equations can be simplified to

$$\rho\frac{Dv_i}{Dt} = -\nabla p_i + \mu\nabla^2 v_i + F_{ext}. \tag{2.3}$$

Each of the four terms of this equation have an intuitive physical meaning. The first term, $\rho\frac{Dv_i}{Dt}$ can also be written as $\rho(\frac{\partial}{\partial t} + v_x\frac{\partial}{\partial x} + v_y\frac{\partial}{\partial y} + v_z\frac{\partial}{\partial z})v_i$. This term gives the rate of change of the velocity of a particle in a fluid as it travels along its trajectory, as opposed to the rate of change at a fixed point in space given by $\frac{\partial v_i}{\partial t}$. The given formulation as $\frac{Dv_i}{Dt}$ is a convention for writing this convective or material derivative.

The next two terms on the right hand side of the equation represent the effect of pressure gradients and viscous diffusion, respectively. This means that the behaviour of flow of this type will be determined by the ratio of pressure gradients to diffusion. Finally, the last term represents the external forcing per unit of volume. For this thesis, we will see this term back as the stirring force used in the simulations, which is described when discussing the setup of the simulation in section 3.3.

Note that the Navier-Stokes equations give no mention of laminar or turbulent flow: both laminar and turbulent flow are described by the equations 2.3. In practice, it is often useful to characterise how strongly a flow is affected by inertial forces versus the viscous forces in order to compare flows with similar characteristics. The Reynolds number is a useful metric for this, and it is defined as

$$Re = \frac{\rho U L}{\mu} = \frac{U L}{\nu}. \tag{2.4}$$

The Reynolds number can interpreted as the ratio of inertial forces, represented by the characteristic velocity U and the characteristic length scale L, and the viscous forces in terms of the viscosity μ. The use of the so-called kinematic viscosity, ν, defined as $\nu = \frac{\mu}{\rho}$, is a common convention in fluid mechanics, combining the fluid properties of viscosity and density.

2.2 Shear flow

In fluids, shear flow is the type of flow characterised by a gradient in the velocity field, as a gradient in the velocity creates a shear by definition. The simplest example would be Couette flow, which describes the motion of a fluid moving between two plates. One of the plates remains at rest whereas the other one moves at a constant speed, causing a shear to form inside the fluid.
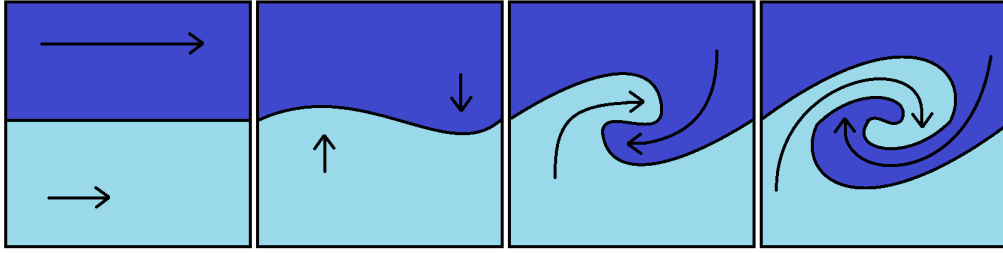
Figure 2.1: Illustration showing a Kelvin-Helmholtz instability in a shear induced by a velocity difference in the two layers of fluid.

Another way shear can appear in fluid flow is in the two-dimensional interaction of either two different types of fluids or a velocity shear in a single fluid. In both cases, slight perturbations can occur on the surface interface. Depending on the density differences, gravity, the wavelength of the perturbations and the velocity differences, the flow can undergo a hydrodynamic instability that the interface. Small perturbations then grow, causing more small perturbations to form at the surface, eventually leading to turbulent mixing of both fluids. This phenomenon is known as Kelvin-Helmholtz instability. Note that the size of these perturbations depends on the viscosity, as more viscous fluids will show less small scale motion and thus smaller perturbations. This does not mean that more viscous fluids are necessarily more stable, as the wavelength of the perturbations determines the stability of the system, not their amplitude.

2.3 Turbulence

Turbulence is an important aspect of fluid mechanics that is present in many types of flow. The flow in pipes, heat exchangers and in the wakes of aircraft are common examples. In particular, turbulence is important when considering an object or fluid in motion with respect to another fluid. As such, turbulence is an important property of flow when studying emulsion flow as well.

Turbulent flow is characterised by its chaotic nature compared to laminar flow, though ordered structures can still be seen in the form of vortex-like swirls called eddies. Despite this, turbulence is not governed by different physics from laminar flow. In principle, the Navier-Stokes equations are just as valid for turbulent flows but the difference lies in the fact that turbulent flows are chaotic and unpredictable. Small uncertainties or inaccuracies in the initial conditions of turbulent flows grow exponentially in time.

This is where laminar flow differs from turbulent flow: for a dynamical system to be considered predictable, the condition is that small changes to the initial conditions of a given system result in small changes in the phase space trajectories in time. Since all measurements have a finite accuracy, it is not possible to exactly predict the flow profile of a turbulent flow because the characteristics of these flows can change drastically under small changes of their initial conditions.

In practice, the Reynolds number discussed earlier gives a useful notion to determine whether a flow will show turbulent behaviour or not. Though the Reynolds numbers at which flow will be turbulent also depend on the flow geometry, the transition between laminar and turbulent flow typically occurs in the range of 10^3 to 10^4, with flow being laminar for Reynolds numbers below this range and turbulence occurring above this range. For the well-studied case of pipe flow, this critical Reynolds number is $Re \approx 2300$. Note that these critical values are not exact, as the Reynolds number is a tool to help describe flow behaviour, not a constant of nature.

Characteristic of turbulent flow is that dissipation of energy occurs only at the smaller scales. Given enough time, all the kinetic energy in a turbulent flow will eventually dissipate, typically

into heat. This can readily be observed when looking at any turbulent flow: unless there is an external force to support the turbulent motion, flow will eventually stop. For example, Kelvin-Helmholtz instability will only continue for as long as there is a velocity shear or two different fluids with a surface interface. Once all fluid is mixed, as a result of the instability, there is no longer a means to sustain the rotational motion caused by the process. This is because the source of the instability, a fluid-fluid interface, is no longer there.

One important result of turbulence theory, the Kolmogorov relation, states that the total kinetic energy, e, of a turbulent flow, scaling with U^2, dissipates as follows:

$$\frac{de}{dt} = -\epsilon_{out}, \qquad\qquad \epsilon_{in} \propto \frac{U^3}{L}, \qquad (2.5)$$

where ϵ is the energy flux per unit of time, with the energy flux ϵ_{out} transferring from larger to smaller scales. A full derivation can, for example, be found in the work of F. Nieuwstadt et al. [9]. On average, these two energy fluxes are equal, though they differ locally based on the local velocity, as by definition the velocity and thus the kinetic energy in a turbulent flow varies in space. The energy is passed on from the macroscale, the scale of the largest eddies in a turbulent flow, to the microscale, the smallest scale in which molecular diffusion becomes relevant. Eq. 2.5 shows that the rate at which energy is transferred from the macroscale to the microscale depends solely on the macroscale properties of the system, i.e. U and L. This corresponds with a timescale of $T = \frac{L}{U}$ for energy to be transferred to smaller and smaller eddies. This process repeats itself until viscous friction transforms the kinetic energy of the small eddies into heat. The associated quantaties for length, time and velocity respectively at the dissipative Kolmogorov microscale are:

$$\eta = \left(\frac{\nu^3}{\epsilon}\right)^{\frac{1}{4}}, \tau = \left(\frac{\nu}{\epsilon}\right)^{\frac{1}{2}}, \upsilon = (\nu\epsilon)^{\frac{1}{4}}. \qquad (2.6)$$

Here, η is known as the Kolmogorov scale. This scale is small enough for viscosity to dominate, as at this scale, molecular diffusion becomes relevant. The large-scale parameters U and L do not directly influence these quantities, and the behaviour no longer depends on the geometry of these system. Only the viscosity ν and the amount of energy dissipated to the small scale, ϵ, matter at the microscale, leading to the expressions in Eq. 2.6.

2.4   Fluid-fluid interfaces

In order to explain the properties of binary emulsions, it is important to discuss the physics at the fluid-fluid interfaces between them. A binary emulsion will typically consist of a dispersed phase and a continuous phase, with the former forming structures inside the bulk of the continuous phase.

Figure 2.2: Example of an oil-in-water emulsion after stirring with a tablespoon. The droplets can be seen to be nearly spherical and do not immediately coalesce despite nearly touching one another due to the inertia still present in the system at the time this picture was taken.

Due to the fluid-fluid interfaces that occur in emulsions, surface effects play an important role. One such property is surface tension, which explains why it is energetically favorable for liquids to minimize their surface area. This can readily be seen from the so-called Laplace tension:

$$\Delta p = \gamma \left(\frac{1}{R_1} + \frac{1}{R_2} \right) \tag{2.7}$$

This equation gives the pressure across a fluid-fluid interface. The surface energy density γ describes the energy per unit of a surface of the liquid, and is a material property for the two materials on each side of the interface. The radii R_1 and R_2 are the two principle radii of curvature, each mutually perpendicular to the liquid surface and to each other. This explains why the structures found in emulsions are typically spherical, as spheres have the lowest ratio of surface area to volume of any shape.

For the practical case of spherical curvature, the right hand side of Eq. 3.8 simplifies to $\frac{2\gamma}{R}$ which, by itself, is also called the capillary pressure and corresponds to the pressure discontinuity in the direction perpendicular to the liquid surface. This implies that the internal pressure inside a spherical droplet of liquid is higher than the internal pressure inside the volume of a completely flat body of water. It should be noted that this equation is not generally applicable, as it assumed a fully uniform density within droplets and assumes that fluid-fluid surfaces are sharp, which is inaccurate when considering phase transitions, for instance.

Eq. 3.8 does, however, provide a useful first insight into fluid-fluid surface interactions, as it explains why a spherical droplet of fluid is an energetically favourable state with a higher pressure compared to the outside of the droplet.

A practical example of this is adding a small amount of oil to water. As oil is insoluble in water, it forms a layer on top of the water due to oil having a lower density than water. Mixing the oil and water suspension will result in an unstable emulsion where the oil forms spherical bubbles inside of water. In this example, oil would be the dispersed phase and water would be the continuous phase. Note that these emulsions are, generally speaking, not stable. In the case of oil and water, the emulsion will revert to the original state, where the oil forms a layer on top of the water. An example of this can be seen in Fig. 2.2.

In the following, we disregard gravity, but even without gravity coarsening would occur

Beyond surface tension, hydrostatic, i.e. gravity-induced, contributions are typically the largest, but as for the Navier-Stokes equation, gravitational effects are not considered here. The remaining surface interactions contributing to the pressure at the surface are called the disjoining pressure. It consists a combination of Van der Waals forces, electrostatic interactions, osmotic effects and structural effects. This means that the disjoining pressure is strongly material dependent. The disjoining pressure is an important part of the methodology to model emulsions which is explained in section 3.3, where the emulsion is made stable through a negative disjoining pressure, preventing droplets from coalescing into one whole as with the aforementioned example of oil in water. A real-world example of this would be an emulsifier or soap, which typically have one hydrophilic and one hydrophobic end. These prevent droplets from coalescing and thus stabilizing the emulsion.

2.5 Droplet formation

The formation, coalescence and breakup of droplets are key processes that determine the stability of an emulsion. In the simulations that we analyse, a statistical balance between coalescence and breakup events occurs, making the emulsion statistically stationary for the given parameters.

In our system, the formation of droplets is a stochastic process that must take place in order to transform a suspension into an emulsion. An example is the stirring of a glass of water and oil, which causes droplets of one liquid to be produced and thus temporarily form an emulsion. The volume fraction is defined as the fraction of the total liquid volume occupied by the dispersed phase. Attempting to add too much material of the dispersed phase to the system causes phase inversion, a process in which the dispersed phase switches roles with the continuous phase. This is analogous to adding so much oil to an oil-in-water emulsion that the system turns into a water-in-oil emulsion, with water droplets inside of the oil.

As explained under section 2.4, fluid-fluid interfaces give rise to surface tension which causes spherical droplets to form. In an unstable emulsion, such as Fig. 2.2, droplets initially form due to the applied stirring force. The initial bulk of oil on top of the water can be interpreted as one large 'droplet' that breaks up into many small droplets due to the inertial stirring force acting on it, breaking up the surface tension. As time goes on, these droplets eventually start coalescing without the stirring force acting on them. Eventually, all the oil will have coalesced, resting on top of the water due to buoyancy. Note that this would not happen in our system, as we disregard gravity: instead, we would see a single large droplet surrounded by water.

There is, however, a secondary effect that also destabilises the emulsion. As two oil droplets are near one another, the effective attractive force caused by surface tension can cause these droplets to coalesce into a single, larger droplet. This can intuitively be understood from Eq. 2.7, as a single large droplet will always have a smaller surface area. This, in turn, means that there is a smaller liquid-liquid interface area, and thus forming a larger droplet is energetically favourable.

This process explains why emulsions are typically not stable. In order to make them stable, a force keeping two droplets apart is needed, as mentioned under the disjoining pressure in section 2.4. An example of this are surfactants, also appropriately called emulsifiers in this context. In the case of oil and water, this surfactant can be a material that is hydrophobic on one end and hydrophilic on the other. This is how the oil and water emulsion present in mayonnaise is stabilised, where several proteins present in egg yolk act as surfactants. This mayonnaise analogy will be expanded on later, as making a dense emulsion computationally is conceptually similar to making mayonnaise at home.

Chapter 3

The modelling of a dense emulsion

Due to the complexity and opacity of binary emulsions, it is extremely difficult or just not feasible to study the physical behaviour of each individual droplet experimentally, nor can the Navier-Stokes equations readily be simulated. In this chapter, the methodology for modelling a binary emulsion is explained, from the computational methods used, to the process of formation of the emulsion itself.

3.1   Methodology

In order to aid the reader in understanding the analyses that will be discussed, we provide here a brief overview of the steps that were taken to perform a statistical analysis of the dispersed phase.

We begin by taking the raw density data from a numerical simulation of a dense emulsion. The relevant details of this simulation are laid out in sections 3.2 through 3.4. The raw data from these simulations are density fields. At the end of this chapter, we discuss the parameters that were varied for the simulations we studied in section 3.5.

This density field is then used to mark the droplets making up the dispersed phase in section 4.1. This, in turn, forms the basis that allows us to track the droplets in time as seen in section 4.2, including any breakup and coalescence events. It is this tracking algorithm that allows us to the analyses we show in chapter 5.

3.2   Lattice Boltzmann Method

The Boltzmann equation describes the dynamics of a gas in terms of probabilities. Since the Navier-Stokes equations are a limit case of the Boltzmann equation, it can be used to describe fluids as well. We discuss it here as it is central to the Lattice Boltzmann Method (LBM) that is used to model the binary emulsions, as a computationally viable alternative to a direct discretization of the Navier-Stokes equations. Two of the main advantages of this method are that the LBM method lends itself well to be parallellized, as is the case for the LBE3D code that is used, and the lack of need to implement a phase-field model. This latter point in particular makes emulsions easier to model, as they naturally contain many fluid-fluid interactions which are more difficult to apply to the Navier-Stokes equations, as there is no collision or interaction term for the small scale interactions of droplets in them.

The idea behind the Boltzmann equation is not to analyse the individual properties of each molecule or particle in a system, but rather do this through the use of probability distribution functions. The macroscopic velocity and density fields can be obtained through local averages,

which is possible due to the individual particles exhibiting Brownian motion (see Eq. 3.5). The probability distribution function $f(\mathbf{r}, \mathbf{v}, t)$ for particles in the six-dimensional space given by the three-dimensional positions $\mathbf{r}$ and velocities $\mathbf{v}$ is given by

$$f(\mathbf{r}, \mathbf{v}, t) = N d\mathbf{r} d\mathbf{v} \tag{3.1}$$

where N is the number of particles in the volume given by $d\mathbf{r}d\mathbf{v}$. The Liouville theorem in classical mechanics shows that this distribution is conserved along flowlines:

$$f(\mathbf{r} + d\mathbf{r}, \mathbf{v} + d\mathbf{v}, t + dt) = f(\mathbf{r}, \mathbf{v}, t), \tag{3.2}$$

without considering possible collisions. To account for collisions between particles, we can write

$$f(t + dt, \mathbf{r} + d\mathbf{r}, \mathbf{v} + d\mathbf{v}) - f(t, \mathbf{r}, \mathbf{v}) = dt \left(\frac{\partial f}{\partial t}\right)_{coll}, \tag{3.3}$$

with a yet undefined collision operator that is a function of f. This can be written in terms of dt, $d\mathbf{r}$ and $d\mathbf{v}$ as

$$dt \left(\frac{\partial f}{\partial t}\right) + d\mathbf{r} \cdot \nabla_r f + d\mathbf{v} \cdot \nabla_{\mathbf{v}} f = dt \left(\frac{\partial f}{\partial t}\right)_{coll}. \tag{3.4}$$

With the acceleration $\frac{d\mathbf{v}}{dt}$ written as $\boldsymbol{\alpha}$ and dividing by dt, we then get

$$\frac{\partial f}{\partial t} + \mathbf{v} \cdot \nabla_{\mathbf{r}} f + \boldsymbol{\alpha} \cdot \nabla_{\mathbf{v}} f = \left(\frac{\partial f}{\partial t}\right)_{coll}, \tag{3.5}$$

which is known as the Boltzmann equation. Here, the term $\mathbf{v}\cdot\nabla_{\mathbf{r}}f$ represents the effect of transport on the probability distribution and the term $\boldsymbol{\alpha} \cdot \nabla_{\mathbf{v}} f$ represents the effect of the applied forcing (as $\boldsymbol{\alpha} = \frac{\mathbf{F}}{m}$). In the used lattice Boltzmann method, the BGK collision operator is implemented [10]. This commonly used operator introduces a relaxation time τ to interpret the collision term $\left(\frac{\partial f}{\partial t}\right)_{coll}$, and is defined as

$$\left(\frac{\partial f}{\partial t}\right)_{coll} = -\frac{f - f_0}{\tau}, \tag{3.6}$$

where f_0 is the equilibrium distribution function corresponding to f, described by the Maxwell-Boltzmann distribution function (not elaborated on here). The right-hand side of Eq. 3.6 states that collisions are treated as a relaxation process towards the equilibrium f_0. Since we are dealing with binary emulsions, however, we must also take into account the interaction forces acting on both components of the fluid:

$$\frac{\partial f_\sigma}{\partial t} + \mathbf{v} \cdot \nabla_{\mathbf{v}} f_\sigma = \left(\frac{\partial f_\sigma}{\partial t}\right)_{coll} + F_\sigma(\mathbf{r}, t). \tag{3.7}$$

Note that this equation applies to each fluid component separately: the subscript σ represents the component of the fluid, i.e. either the continuous or the disperse phase of the binary emulsion.

3.3   Modelling binary emulsions

The Lattice Boltzmann Method (LBM) is a relatively new [11] method for doing fluid simulations. Other methods to discretize the Navier-Stokes equations include the finite volume method and the finite element method. The LBM in particular is a flexible and computationally efficient method that has proven to be well-suited to model the flow behaviour of multiphase systems, and 3D systems in particular [11]. The LBE3D code is a parallel implementation of the LBM method [12], which in particular is able to model surface effects like surface tension and the disjoining pressure [4][13][14] due to its implementation of the forcing term F_σ in Eq. 3.7.

In the case of this study, the goal is to analyse the physical phenomena that relate to the macroscopic interactions between two phases of an emulsion in a fairly simple, triple periodic geometry. The boundaries of this geometry are continuous: the geometry consists of a cube of 512 grid points in all three spatial directions (i.e. each face of this cube connects to the face at the other end of the cube). As such, fluids are considered to be a continuum, disregarding the interactions that occur at a molecular level.

However, in order to model droplets in an emulsion, it is necessary to include a model for surface tension and the disjoining pressure in the simulation model, which appear as two inter-particle forces, in contrast to the above. This is because both of these microscopic effects greatly influence the macroscopic behaviour. The surface tension comes from a repulsive force between the two phases of the emulsion in the LBE3D method that was used [4]. This model was based on the Shan-Chen pseudo-potential approach for multiphase flows [15], such as the ones we study here. It is given by:

$$F_\sigma^{(r)}(\boldsymbol{x}) = -\mathcal{G}_{AB}\varphi_\sigma(\boldsymbol{x};t) \sum_{a,\sigma'\neq\sigma} w_a \varphi_{\sigma'}(\boldsymbol{x}+\boldsymbol{c}_a;t)\boldsymbol{c}_a \tag{3.8}$$

where the phase separation occurs due to the potential φ_σ being taken equal to the density ρ_σ, which differs for both components. Note that this forcing only applies to all its directly neighbouring particles. Here, $\mathcal{G}_{AB}$ is the magnitude of the forcing, w_a is a set of weights for the applied LBM scheme and $\boldsymbol{c}_a$ are the streaming velocities, a parameter in the probability distribution in the LBM scheme alongside the position $\boldsymbol{x}$ that represents the velocity a particle would have without collisions or other interactions.

With just this additional forcing term alone, however, droplets that form due to surface tension would not be stable due to the dominant attractive forces for fluid of the same component. To account for this, a disjoining pressure term was also introduced that applies also to the second neighbours, i.e. including the neighbours of the neighbours of a particle. This creates a balance with the above force to prevent the whole system from coalescing. This introduces a repulsive force between particles of the same component:

$$F_\sigma^{(F)}(\boldsymbol{x}) = -\mathcal{G}_{\sigma\sigma,1}\psi_\sigma(\boldsymbol{x};t) \sum_{a\in NN} w_a \psi_\sigma(\boldsymbol{x}+\boldsymbol{c}_a)\boldsymbol{c}_a - \mathcal{G}_{\sigma\sigma,2}\psi_\sigma(\boldsymbol{x};t) \sum_{a\in NNN} w_a \psi_\sigma(\boldsymbol{x}+\boldsymbol{c}_a)\boldsymbol{c}_a \tag{3.9}$$

where NN represents a particle's neighbours, and NNN represents both its neighbours and its second neighbours. This way of modelling surface tension and disjoining pressure was adapted from the work of Benzi et al. [16], and proven to be valid for the mesoscopic simulations that we consider here (see, for example, the work of Benzi et al. [17]). In the model, the sum of these two forces form the forcing term F_σ in Eq. 3.7.

In addition to these two interaction forces, an external stirring force is applied to the emulsion in order to mix the two fluids. The stronger an inertial force like this is, the smaller the droplets that will be formed due to inertial forces beating out the surface tension that keeps a droplet together. To ensure an isotropic forcing field for random mixing, the stirring force has the shape of a sum of sine waves with small wavenumbers. For each spatial direction i, the stirring force F^α is given by:

$$F_i^\alpha(\boldsymbol{x},t) = A\rho^\alpha \sum_{j\neq i}[\sin(k_j x_j + \Phi_k^{(j)}(t))], \tag{3.10}$$

where $i,j = 1,2,3$, A is a parameter controlling the amplitude of the forcing and the wave-vector components k_j are chosen such that $k^2 = k_1^2 + k_2^2 + k_3^2 \leq 2$. The phases $\Phi_k^{(j)}$ come from independent Ornstein-Uhlenbeck processes, a random process similar to a random walk.

3.4   Making the emulsion

The initial setup for every simulation is a flat interface of the two fluid components. The emulsification process proceeds thanks to the applied stirring force of Eq. 3.10, which causes this interface to break. The fluids will subsequently split into a continuous phase and a dispersed phase. The latter can be tracked as individual droplets and forms the focus of this research.

However, this process is complicated when making dense emulsions, where the volume fraction of the dispersed phase is more than 50%, i.e. there is more fluid of the dispersed phase than there is of the continuous phase. Creating a dense emulsion is difficult because of phase inversion. This is why making mayonnaise is difficult: in this process, oil needs to be added evenly while mixing. In the simulations, this process of increasing the volume fraction of the dispersed phase is done similarly, in that the methodology ensures that the added volume of dispersed phase is distributed evenly to prevent phase inversion, a process where the continuous and disperse phases swap. During each LBM time step, material of the dispersed phase (denoted with a subscript 1) is added uniformly to each droplet. In order to maintain incompressibility, it is necessary to simultaneously remove fluid from the continuous phase (denoted with a subscript 2), which is also done uniformly in accordance to the amount that was added for the dispersed phase. If the total volume of the system is given by $V = M_1\rho_1 + M_2\rho_2$, then the addition and removal of both respective components should be such that $M_1\rho_1 + M_2\rho_2 = \alpha M_1\rho_1 + \beta M_2\rho_2$, where α and β are defined as

$$\alpha = 1 + \delta \beta = 1 - \left(\frac{M_1}{M_2}\right)\delta, \tag{3.11}$$

to ensure the total volume remains constant. The free parameter δ determines how rapidly this process of increasing the volume fraction takes place. Unless mentioned otherwise, all simulations in this thesis used a value of $\delta = 1.25 \cdot 10^{-6}$ for a varying number of time steps. From here on, this process will be referred to as pumping. The desired volume fractions were reached by starting from a flat interface with an initial volume fraction of 30% for all simulations. This volume fraction thus gradually increases for a number of timesteps T_{pump} that is set as a parameter to reach the different volume fractions given in section 3.5.

After this period of pumping, the system is left to rest, during which the number of droplets drastically decreases. During this time, most droplets coalesce, as the surface tension becomes more significant than the inertia that would prevent droplets from coalescing. This happens independently of the initial conditions of the system, which include changing the volume fraction of the phases of the emulsion and changing the applied initial forcing strength. After enough droplets have coalesced, the number of droplets stays roughly constant for an extended period of time, and few coalescence and breakup events occur during this stage. Due to the fact the number of droplets stays roughly constant in this state, it is ideal to use for studying the behaviour of the dispersed state. It should be noted, however, that this does not necessarily mean few breakup and coalescence events happen; in fact, many such events happen for the high volume fraction cases, but these events average out. This whole process is illustrated in Fig. 3.1.
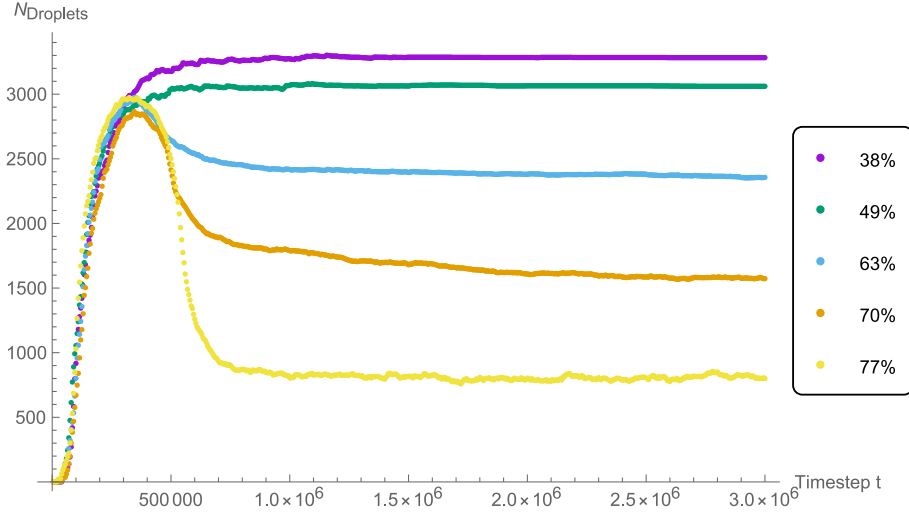
Figure 3.1: Graph of the number of droplets in time for simulations with different volume fractions. The initial period of pumping can be seen, after which the amount of droplets decreases based on the volume fraction reached, with the higher volume fractions resulting in fewer, larger droplets.

3.5   Simulation parameters

Now that the process of setting up the binary emulsion is explained, we can now discuss the choice of parameters for the simulations. By changing only one property for each simulation, the overall effect that that property has on the physics of the system can be looked at. In particular, five simulations with a varying volume fraction and five simulations with a varying stirring force will be considered in the following. All other parameters not explicitly mentioned are the same within these two sets of simulations. The relevant parameters are laid out in Table 3.1 and Table 3.2.

As explained above, however, the system does not immediately reach the desired state. Especially for the high volume fraction cases, it takes time for the system to reach a semi-stable state that can be analysed with good statistics. Depending on the chosen initial conditions of the system, this state is either fully stable, or the system eventually undergoes a phase inversion, in which the continuous and dispersed phases switch. This phase inversion is not elaborated on

Volume fraction	L	$\delta \cdot 10^{-6}$	T_{pump}	$\text{A} \cdot 10^{-6}$	$\langle N_{Droplets} \rangle$
38%	512	1.25	114900	0.485	3283
49%	512	1.25	289900	0.485	3061
63%	512	1.25	439900	0.485	2356
70%	512	1.25	504900	0.485	1573
77%	512	1.25	559900	0.485	800

Table 3.1: Table showing the parameters in the simulations with varying volume fraction. The grid size L, the pumping strength δ, as described in section 3.4 and the strength of the stirring force A (see Eq. 3.10) were kept constant. In order to achieve the various volume fractions, only the time step at which the pumping is stopped, T_{pump}, was changed. $\langle N_{Droplets} \rangle$ shows the average number of droplets over the time period between 2-3 M time steps, during which the number of droplets stays roughly constant, as can be seen in Fig. 3.1.

Volume fraction	L	$\delta \cdot 10^{-6}$	T_{pump}	$A \cdot 10^{-6}$	$\langle N_{Droplets} \rangle$
77%	512	1.25	559900	0.405	967
77%	512	1.25	559900	0.425	911
77%	512	1.25	559900	0.455	861
77%	512	1.25	559900	0.485	800
77%	512	1.25	559900	0.505	761

Table 3.2: Table showing the parameters in the simulations with varying stirring force strength. The grid size L, the pumping strength δ, as described in section 3.4 and the time at which the pumping is stopped, T_{pump}, were kept constant. Only the stirring force strength was changed here, resulting in slightly fewer droplets on average for the cases with a stronger forcing. $\langle N_{Droplets} \rangle$ shows the average number of droplets over the time period between 2-3 M time steps, during which the number of droplets stays roughly constant. The case with a stirring force of $0.485 \cdot 10^{-6}$ is shown as the 77% volume fraction case in Fig. 3.1; the others are not shown here, but look virtually the same.

here, but it is why the given forcing strengths in Table 3.2 were chosen, as these values are around the point where this phase inversion occurs. Unless stated otherwise, the time range used for the following analysis takes place in this semi-stable state, in practice between $t = 10^6$ and $t = 3 \cdot 10^6$.

Chapter 4

Tracking algorithm

4.1   Marking the droplets for tracking

The raw data from the simulation results is a density field for each time step. At each position in the grid, the density information from the simulation was used to distinguish both phases of the emulsion. In practice, there is always a slight overlap between the low and high densities corresponding to each component. A cut-off value for the density of 0.68 was chosen, between the densities of each component of 0.18 and 1.18, respectively for the continuous and dispersed phases. (The viscosity of both phases were taken to be equal, making the density the only material difference between the two phases.) This value of 0.68 corresponds to the edge of the droplets, which are considered to be sharp boundaries. Droplets are thus defined as clusters of points with a density close to the bulk value. All of these droplets are then assigned a unique number via a colouring algorithm to distinguish them from one another.

The next step is to make sure that this assignment of names for each droplet stays consistent in time. This allows for proper tracking of the droplets, allowing for individually following them over time. Additionally, the number of droplets present in each time step does not stay constant. Droplets can breakup into two or more droplets and, conversely, they can also coalesce. Due to the large amount of data involved, however, the density information was not dumped at every simulation time step, but rather once every 100 time steps. In the following, 'one dump step' refers to 100 simulation time steps.

For many of the statistics given in the results, it proved useful to also define the 'neighbours' of each droplet at every point in time. To do this, a Voronoi decomposition was done using the centre of mass of each droplet. Each Voronoi cell that borders a droplet's own cell is then considered to be a neighbour for that time step. Note that the choice to do the Voronoi decomposition from the centre of mass of each droplet is not perfect, as it implicitly assumes all droplets are spherical, which is not true. However, this has no bearing on the statistics that we use the centre of mass for.

4.2   Tracking

After labelling the droplets at each time step, a tracking algorithm is applied. The basic idea of the tracking is to compare the overlap between the volume of a droplet at a given time step with the volumes of droplets in the next dump step, as in Eq. 4.7. This overlap is computed by first rearranging the density data to 1s and 0s, with the 1s corresponding to the dispersed phase and the 0s corresponding to the continuous phase. The volume of a droplet can now be measured as points in a grid with density 1, that is to say $V_{droplet} = N_{gridpoints}$. In most cases, the grid points that make up a droplet should be nearly the same in the following time step, as the velocities are

small relative to the grid size. The first step of the tracking algorithm is to compute an overlap matrix, where the grid points from a droplet at one time step are compared to the grid points from all droplets in the next time step. For clarity, the droplet that is being compared with at a given time step is called the 'reference droplet', and the droplets that possibly overlap with it in the following time step are called 'candidate droplets'. In a formula,

$$V_{overlap}(t) = V_{reference}(t) \cap V_{candidate}(t+1). \tag{4.1}$$

In most cases, a single candidate droplet will have a large overlap with the reference droplet, in which case the droplet is consolidated, meaning that we can now label the candidate droplet as being one and the same as the reference droplet. A two-dimensional sketch of this process is given in Fig. 4.1.

The choice of the cut-off for what is considered a large enough overlap to ensure a droplet is being tracked correctly is based on the possible inaccuracies in this process. There are three reasons the tracking cannot perfectly match the volumes in between time steps: first of all, droplets will move with their velocity over the course of a time step, causing a slight discrepancy in the overlap volume. Secondly, the droplet itself can slightly deform due to the forces working on it or collisions with nearby droplets. Finally, due to the discrete grid points used, the measured volume itself varies slightly. Even a perfectly spherical droplet moving only in one Cartesian direction would have a slightly oscillating volume, as the amount of grid points that overlap with it varies slightly in time. All three of these effects can be seen in Fig. 4.1.

The first of these three issues can largely be fixed by applying a Kalman filter. Since we know the velocities of the grid points through the LBM method, we can estimate the velocity of the center of mass of droplets at any time step by averaging the velocity of all the points within its volume. This allows us to increase the accuracy of the overlap matrix by extrapolating the grid points to be compared with by this velocity value. This is shown in Fig. 4.2.

This approach is not perfectly accurate, as the centre of mass of candidate droplets will never exactly overlap with the predicted value using the velocity of the reference droplet. In practice, there are two checks to ensure that a droplet is being tracked correctly. The first of these is checking the percentage of the largest overlap. For most droplets, the volumes of several droplets will make up the grid positions at the original time step. The first check makes sure that the largest of these overlaps is at least 20% and then only considers this droplet of largest overlap as a candidate for the consolidation. While this value may seem very low, the second check makes sure that the correct droplet is checked, both to reduce errors and reduce the computational time required.

$$\frac{V_{overlap}(t)}{V_{reference}(t)} \geq 20\% \tag{4.2}$$

$$\frac{|V_{candidate}(t+1) - V_{reference}(t)|}{V_{reference}(t)} \leq 10\% \vee |V_{candidate}(t+1) - V_{reference}(t)| \leq 200. \tag{4.3}$$

The second check looks at the actual volume that the candidate droplet's volume is either within 10% of the volume of the droplet at the initial time step, or within 200 grid units. This number of 200 is very small compared to the total number of grid points, which equals $512^3 = 1.34 \cdot 10^8$. The latter check was implemented to ensure that very small droplets can also be tracked properly, as in practice, very small droplets with a volume of around 100 grid points could have their volume fluctuate for more than 10% over the course of one dump step due to the three effects mentioned above. Different cut-off points were tested and do influence the outcome of the tracking. Choosing the cut-off percentage too strictly, for example by enforcing the volume to be accurate within 1%,

Simulation	$\langle N_{tracked\,droplets} \rangle$	$\langle N_{droplets} \rangle$	Avg. error (absolute)	Avg. error (%)	σ (absolute)	$\sigma(\%)$
I512V38	3283.71	3283.71	0	0	0	0
I512V49	3063.48	3063.48	0	0	0	0
I512V63	2372.86	2372.87	0.01	$2.19 \cdot 10^{-4}\%$	0.09	0.004%
I512V70	1591.12	1591.15	0.03	$1.97 \cdot 10^{-3}\%$	0.21	0.013%
I512V77	806.21	806.38	0.21	$2.59 \cdot 10^{-2}\%$	0.54	0.067%

Table 4.1: Error rate of the volume fraction simulations. The real number of droplets here is given by the marking of the droplets described in section 4.1.
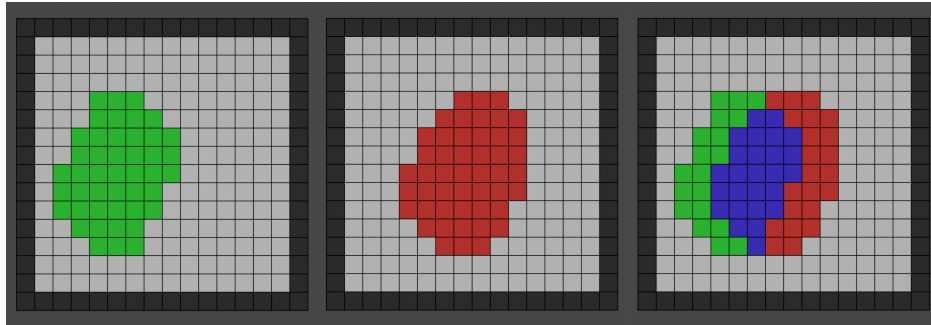

Figure 4.1: 2D sketch of a tracking event of a droplet, in the simplest case of a consolidation. The left image shows a droplet at an initial time step. One time step later, it moves slightly according to its velocity and changes shape based on the forces acting on it. This is shown in the middle image. The final image shows the overlap between these two images, which gives a large overlap between the two.

causes some droplets to not be tracked properly due to the inherent limitations mentioned, whereas choosing the cut-off percentage too widely causes droplets to be tracked erroneously. It is possible to know how effective the tracking is because we already can know the exact number of droplets that exist on each time step from the earlier marking of the droplets. The chosen values produce very few errors, as can be seen in Table 4.1. Despite this good result, however, it should be noted that this error does add up. For instance, for the most extreme case of a 77% volume fraction, the average error per time step of 0.21 means that there are around 2000 instances where droplets are not tracked properly over the course of 1M time steps (as the tracking algorithm checks only once per time dump step).

During the tracking process, there will be cases where no candidate droplet that passes both the checks is found. In these cases, the reference droplet in question must either coalesce with another nearby droplet into a single bigger one, or it breaks up into two smaller droplets over the course of this time step. Should the aforementioned conditions for consolidation of a single droplet fail, the tracking algorithm then checks to see if the same conditions are fulfilled for either a coalescence or a breakup event.

For coalescence to occur, both the reference droplet and the neighbour at the same time step with the biggest volume need to individually pass the first check. This does not matter for most coalescence events, but it is crucial for very small droplets to be able to coalesce with big droplets, as the droplets use their own volume for the first check with a threshold of 20%. For example, in the case where two droplets of volumes 9900 and 100 coalesce, the volumes of the droplets at the initial time step, 9900 and 100, is used instead of the total volume of 10000 for the first check. After this check, the second check is performed by comparing the sum of the two volumes at the initial time step to that of the candidate droplet in the next time step.
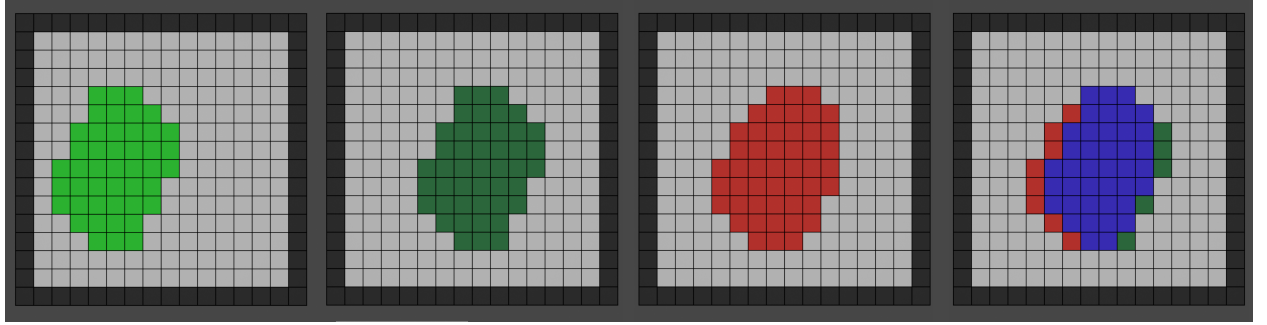
Figure 4.2: 2D sketch of a consolidation event of a droplet with the Kalman filter applied. The left image shows a droplet at an initial time step. In order to better overlap the volume, the velocity of the center of mass of the droplet is added to each grid point, shown in the second image. One time step later, the droplet moves slightly according to its velocity and changes shape based on the forces acting on it. This is shown in the third image. The final image shows the overlap between the initial droplet with the Kalman filter applied and the droplet in the next time, which gives a much better overlap compared to 4.1, causing the algorithm to check if this overlap is significant enough to be considered a consolidation.
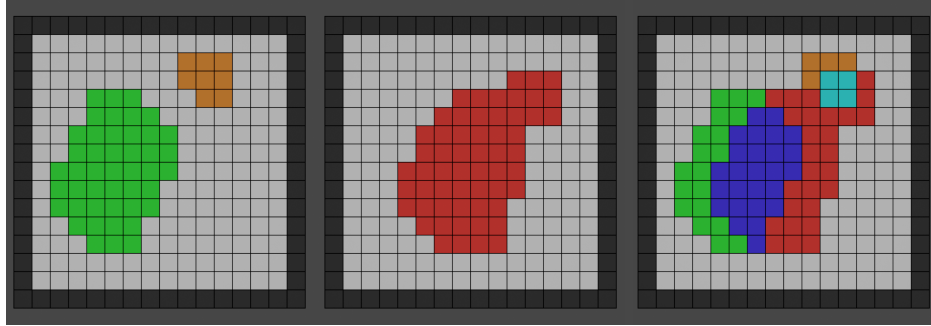

Figure 4.3: Sketch of the way the tracking algorithm handles a coalescence event. The image on the left shows two droplets nearby at one time step in green and orange. The middle image shows that a larger droplet is at roughly the same position in the next time step. The image on the right shows what the tracking does in this case: it overlaps the original green and orange droplets and finds significant overlap with the red droplet of the new time step. This overlap is coloured in dark blue for the green droplet, and light blue for the orange droplet.

Conditions for coalescence:

$$\frac{V_{overlap}(t)}{V_{reference}(t)} \geq 20\% \ \wedge \ \frac{V_{overlap}(t)}{V_{neighbour}(t)} \geq 20\%, \tag{4.4}$$

$$\frac{|V_{candidate}(t+1) - (V_{reference}(t) + V_{neighbour}(t))|}{V_{reference}(t) + V_{neighbour}(t)} \leq 10\% \tag{4.5}$$

or

$$|V_{candidate}(t+1) - (V_{reference}(t) + V_{neighbour}(t))| \leq 200. \tag{4.6}$$

This process is essentially reversed for breakup events. For the first check, the sum of the volume of the two candidate droplets with the largest overlap is used. Contrary to the coalescence case, their sum should be larger than 20%, similar to the consolidation case. For the second check,
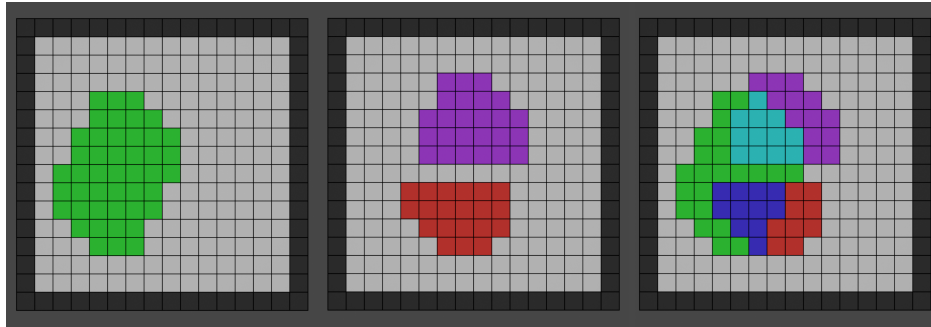
Figure 4.4: Sketch of the way the tracking algorithm handles a breakup event. The image on the left shows an example droplet in green. The middle image shows the next time step, where this droplet breaks up into two smaller droplets coloured red and purple. The final image overlaps the previous two, showing the areas of overlap with the red and purple droplets respectively in dark and light blue.

the sum of volumes of the two candidate droplets is compared to the volume of the reference droplet.

$$V_{overlap}(t) = V_{reference}(t) \cap V_{candidate_1}(t+1) + V_{candidate_2}(t+1). \tag{4.7}$$

Conditions for breakup:

$$\frac{V_{overlap}(t)}{V_{reference}(t)} \geq 20\%, \tag{4.8}$$

$$\frac{|(V_{candidate_1}(t+1) + V_{candidate_2}(t+1)) - V_{reference}(t)|}{V_{reference}(t)} \leq 10\% \tag{4.9}$$

or

$$|(V_{candidate}(t+1) + V_{candidate_2}(t+1)) - V_{reference}(t)| \leq 200. \tag{4.10}$$

This process is repeated for each time step. Droplets are labeled as the same number as long as they continue to consolidate. Once a coalescence or breakup event happens, that number will no longer be used by any droplet for the rest of the tracking, and instead the 'new' droplets are given new numbers, incrementing from the highest current number used. The data that is output comes in two forms, Lagrangian and Eulerian. The Lagrangian data contains all the information per individual droplet for all time dump steps and the Eulerian data instead contains all the information per time dump step for all individual droplets that exist at that time dump step. This makes the data very flexible, and it is relatively easy to do different kinds of analyses on the data, as will be shown in chapter 5.

One limitation of this tracking strategy is that it is impossible to tell if a coalescence or breakup event involves only two droplets. Especially for breakup events, it seems reasonable to think that there are events where droplets split up into three or more droplets at once, though rare. This is why the tracking happens separately from the colouring: the colouring gives us the information of the existence of each droplet at every time step, and thus, it is possible to check if the coalescence and breakup events the tracking procedure finds is correct. Even with this limitation, however, 4.1 shows that the tracking is very accurate as is.

Chapter 5

Statistics of droplet dynamics

Using the procedure described in Chapter 3 on the simulations described in section 3.5, we have a lot of data on the droplets in both a Eulerian and a Lagrangian format. In this chapter, this data is used to analyse the behaviour of the droplets. Many different types of analysis are possible on this large data set. In this thesis, a few options were chosen in order to characterise the flow and learn about how the behaviour of the droplet differs for especially high volume fractions compared to less dense emulsions. It should be noted, though, that much more is possible with the data as is.

We first look at the trajectories of the droplets in section 5.1. Visualising these trajectories helps to identify features in the geometry where droplets move or accelerate in certain directions. This allows us to see if the motion is truly laminar for high volume fractions, if they exhibit turbulent motion in some way, or if some unexpected behaviour occurs.

The large amount of data also allows us to get statistics on the dynamics of droplets. The most basic of these is a probability distribution of the velocities and accelerations of droplets, which is reported in section 5.2. Compared to similar cases, the probability distributions differ significantly from a normal distribution. We further discuss why this is likely caused by an anisotropy in the stirring force.

As we have information of the positions of droplets at all time dump steps, we can compute statistics on the rate at which a droplet's position is no longer correlated with its position at an earlier time. Since we also have information on the neighbours of each individual droplet, we can track and compare them to see the time scale at which a droplet moves away from its neighbours as well. Both of these points are discussed in section 5.3. A similar analysis on the velocity of droplets, the Lagrangian structure function, is discussed in section 5.4.

Finally, the data was used to implement a statistical framework from a paper [18] in section 5.5.

By using the distances between two neighbouring droplets, a velocity gradient field was computed and visualized. This approach, shown in section 5.5, closely follows the statistical framework from the work of Graner et al. [18]. While this is but a small part of what is suggested in the aforementioned paper, it shows that this framework can be applied for the used methodology for studying dense emulsions.

5.1 Trajectories

The trajectories of droplets represent the path along which their centers of mass travel in time. By looking at the way individual droplets move and accelerate, we can see to what kind of motion they exhibit qualitatively. Since the stirring force given by Eq. 3.10 was designed to be random
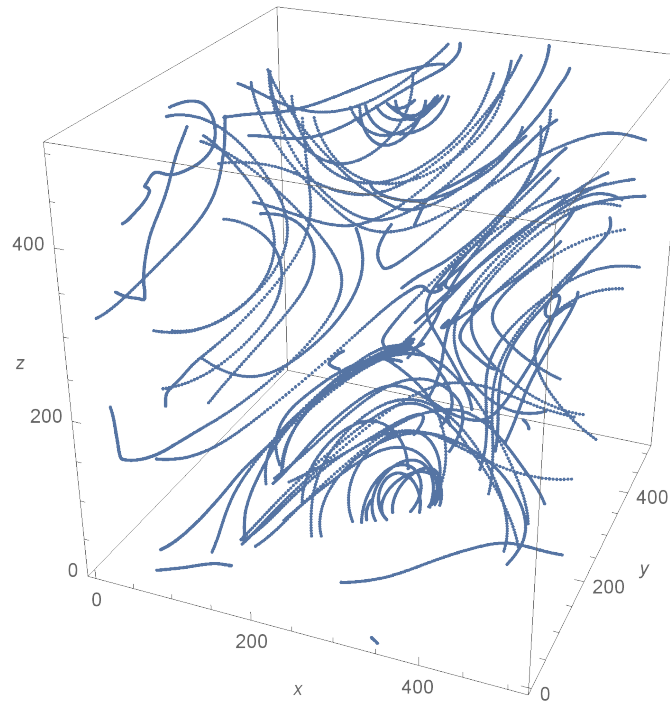
Figure 5.1: Example trajectory of droplet 1737 for the 38% volume fraction simulation for its entire lifespan.

and isotropic, the trajectories can give a first insight in the flow behaviour of the droplets. The expectation here is that droplets show a combination of Brownian motion, possibly in addition to an advective translating motion of clusters of droplets.

The trajectories are computed by taking the position of any single droplet for many different time dump steps of the Lagrangian data and plotting those points. An example is given in Fig. 5.1. All the trajectories are continuous due to periodic boundary conditions, hence the cubic shape of the graph. This also means that droplets can be correlated with positions they were earlier at, but one or more box lengths away in any direction.

Trajectories such as the one given in Fig. 5.1 all show circular patterns of around half the box size, suggesting that the droplet flow is following a zero average flow field. Given the supposed anisotropic nature of the only external force, Eq. 3.10, this is unexpected. This is covered in detail in section 5.2.

Figure 5.2 shows the spread of droplets in time, illustrating the trajectories of many droplets at once. It also shows the longevity of droplets before they breakup or coalesce: as mentioned in 4.2, droplets are given a new identifying number whenever they undergo breakup or coalescence, causing them to disappear from this graph. For the low volume fraction case, very few breakup and coalescence events happen throughout the chosen time range of 1-2M time steps, causing almost all of the droplets to remain visible for the entire duration. The opposite is true for the high volume fraction case, where only a few droplets will not have broken up or coalesced in this time frame.

(a) Volume fraction 38%
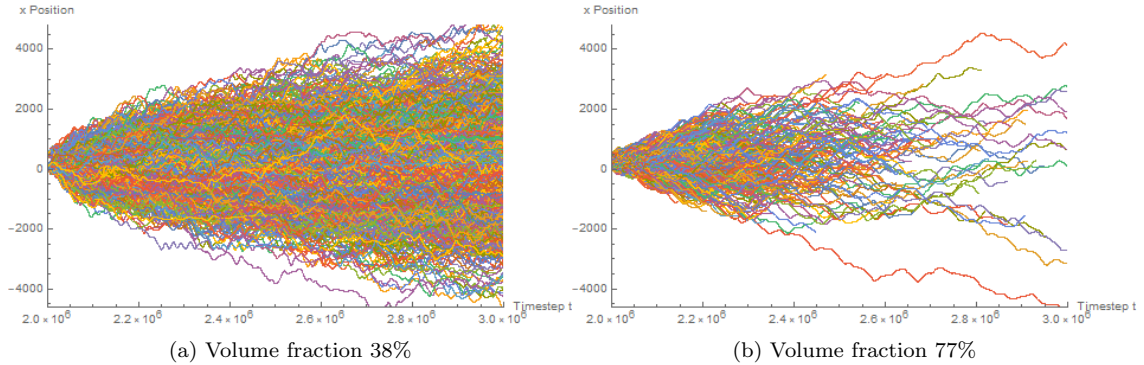
(b) Volume fraction 77%

Figure 5.2: Example of the x-coordinate as a function of time for all droplets that existed at $t = 2 \cdot 10^6$ for two of the volume fraction cases. The time range given is between 2-3 M time steps. Droplets that undergo either coalescence or breakup are no longer considered from the time step the event happens.

5.2 PDFs

The Eulerian data can be used to characterise the velocity field of the fluid as a whole, especially by averaging over many time steps. The velocity distribution can be computed by taking a histogram of this velocity data. Normalizing the histogram to 1 then gives the probability distributions of the velocity. These probability density functions (PDFs) give a quantitative representation of the velocities in the simulations. Looking at these PDFs is useful to see the effect of the volume fraction on the velocity distribution of droplets, and the flow of the system as a whole. We expect to see a Gaussian distribution, corresponding to the random motions induced by the applied forcing. For larger volume fractions, however, the system becomes increasingly crowded, which could impact the velocity distribution.

The PDF for the velocity in the x-direction of droplets for various volume fractions is given in Figure 5.4. Note that the root mean square velocities were used for this figure to emphasize the similar structure of the PDFs, regardless of volume fraction. The PDFs resemble a Gaussian distribution for smaller velocities, but all volume fractions show a steeper slope for high velocities than would be expected for a normal distribution. The higher volume fractions in particular show a strong falloff in probability for around velocities of around $2 \cdot v_{rms}$. In the context of the result of the relative dispersion graph (see Fig. 5.4), the lack of space for droplets to move around seems to decrease the probability of high velocities, which would explain the skewed nature of the velocity PDFs. This could explain why this behaviour is more defined for high volume fractions.

The 77% volume fraction case was fit using a triple Gaussian, with one peak at $v = 0$ and the two other peaks at this apparent falloff point in both directions:

$$P_{fit}(v) = A_1 e^{-\sigma_1 \left(\frac{v}{v_{rms}}\right)^2} + A_2 e^{-\sigma_2 \left(\left(\frac{v}{v_{rms}}\right) - \mu\right)^2} + A_2 e^{-\sigma_2 \left(\left(\frac{v}{v_{rms}}\right) + \mu\right)^2}, \tag{5.1}$$

with the amplitudes A, standard deviations σ and the falloff point μ as fit parameters given in the appendix, see Fig. A.1.

One possible explanation for this triple Gaussian could lie in the way droplets move away from their neighbours for the high volume fraction case. Due to the lack of mobility, droplets could exhibit a sort of caging effect, where droplets are trapped by their neighbours until a strong enough force causes them to eject away from their 'cage'. This idea is sketched in Figure 5.3. This caging effect would also suggest the standard deviation of the velocity would be higher for higher volume
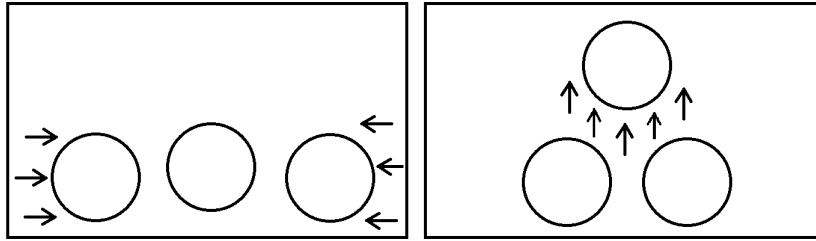
Figure 5.3: Sketch of the possible caging effect, where the idea is that a droplet may get pushed out with a high acceleration by its neighbours. Note that in the actual simulations, the droplets are much more closely packed than in this sketch.

fractions, however, and this is not the case. As such, it cannot be confirmed that this caging effect strongly affects the shape of the PDF or if it happens at all.
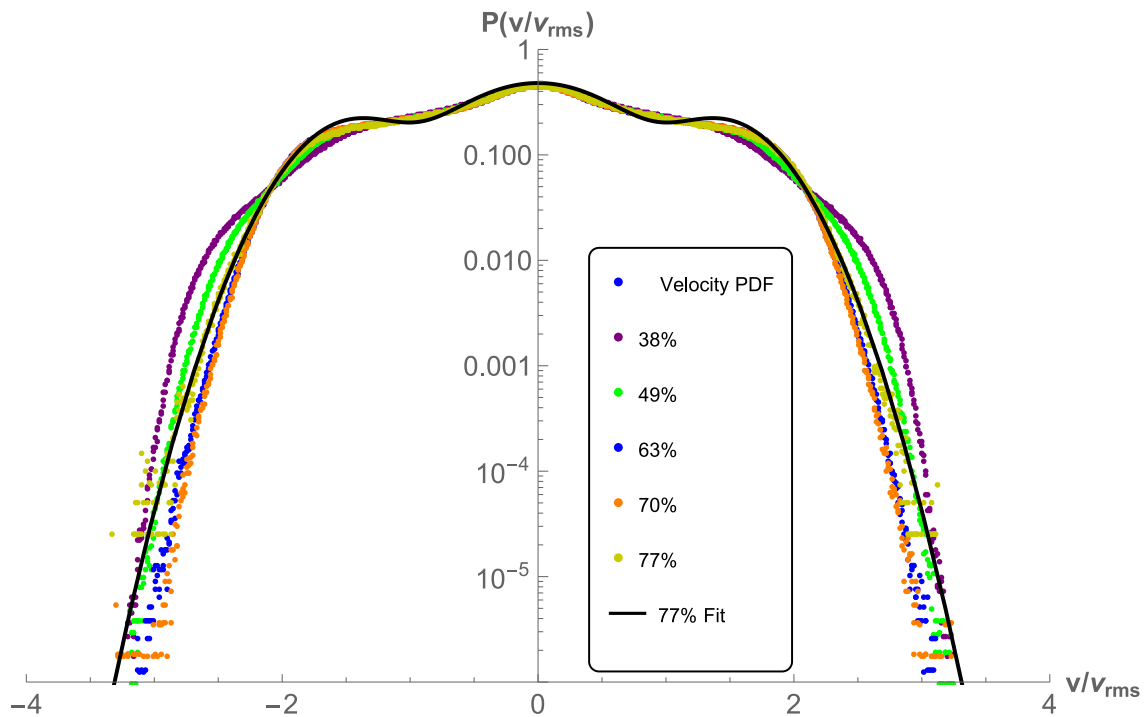

Figure 5.4: Normalised plot of the probability distribution of the velocity of droplets for the simulations with varying volume fractions. The time intervals used were between 1-3 M time steps, which corresponds to the statistically stable period (see Fig. 3.1). The integral is normalised to one, and the velocity is divided by the root mean square velocity of the droplets given in 5.1.

Another potential cause of the deviation from a normal distribution lies in the fraction of droplets of which the velocity aligns with the diagonal vector (1,1,1) in both directions, as found in the discussed trajectories. This prevalence can be exemplified by considering the solid angle, which shows that this difference occurs for all droplets in the same fashion. This was done by calculating the angle difference between the vector (1,1,1) and the velocity vectors and making a histogram of the result, in a similar fashion to the PDFs of the velocity. The result for one specific simulation is given in Figure 5.5 alongside similar histograms for two vectors mutually perpendicular to (1,1,1). This was done for all volume fraction simulations, the simulations varying the stirring force and an additional test case where the phases term $\Phi_k^{(j)}(t)$ from Eq. 3.10 was

Volume fraction	38%	49%	63%	70%	77%
$v_{rms} \cdot 10^{-2}$	2.83	2.52	2.14	1.87	1.72

Table 5.1: Values of the root mean square velocity for the simulations where the volume fraction was varied (see Table 3.1).

Volume fraction	38%	49%	63%	70%	77%
$a_{rms} \cdot 10^{-4}$	8.12	6.45	4.94	3.97	3.46

Table 5.2: Values of the root mean square acceleration for the simulations where the volume fraction was varied (see Table 3.1).

set to zero, and it showed the same general shape for all cases. This was done to prove that the parametrization of the sinoid part of 3.10 is what causes this behaviour.

This prevalence is a result of the applied forcing on the system given by Eq. 3.10. A check was done to verify this using a test simulation where the phases term in the stirring force was set to zero, which gave virtually the same result for the PDFs. This means that there was a mistake in the parametrization the initial conditions of the simulations. The wave numbers k in the sine in this equation did not produce a completely isotropic force field as was intended.

The corresponding PDFs for the acceleration, shown in Fig. 5.6 fit well using a stretched exponential distribution of the form:

$$P(a) = C \cdot e^{-\frac{\left(\frac{a}{a_{rms}}\right)^2}{(1+|\frac{a\beta}{a_{rms}\sigma}|^\gamma)\cdot\sigma^2}}. \tag{5.2}$$

Compared to the other volume fractions, the 77% case stands out for having a higher probability for higher accelerations.
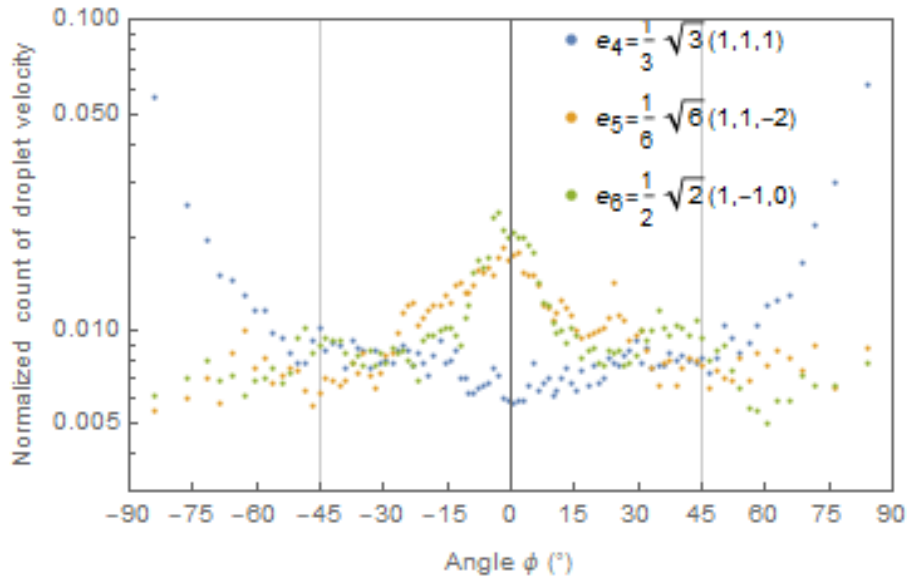
Figure 5.5: Normalised plot of the distribution of velocity vectors of droplets using the solid angle with different bases for the 70% volume fraction case. Here, 0 degrees corresponds to vectors perpendicular to the used basis, whereas 90 and -90 degrees correspond to the vector itself or its reverse, respectively.
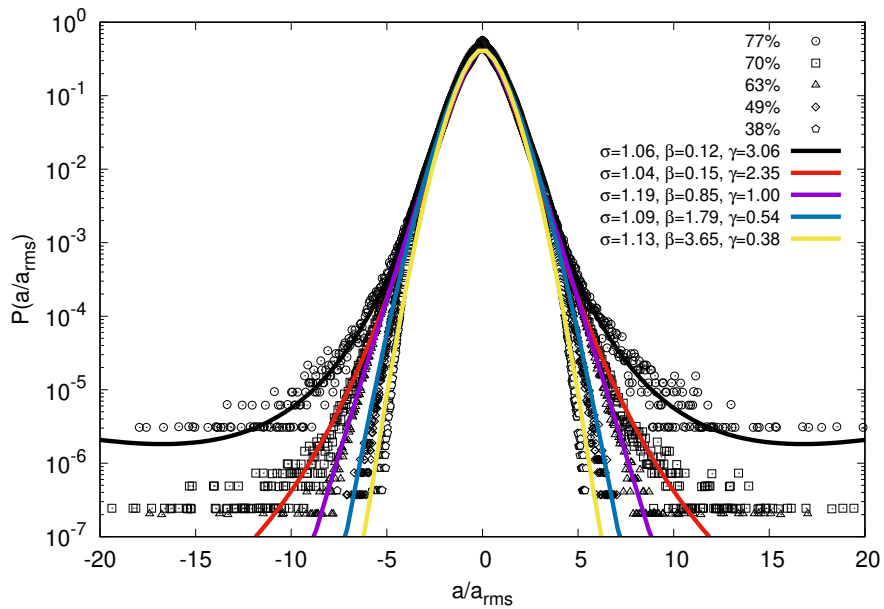

Figure 5.6: Normalised plot of the probability distribution of the acceleration of droplets for the simulations with varying volume fractions. The time intervals used was between 1-3 M time steps, and the acceleration is divided by the root mean square acceleration of the droplets given in 5.2.

5.3 Dispersion

Looking at the position of droplets relative to their position at an earlier time step is another way to learn more about the transport due to the flow field. This allows us to know the time scales at which the droplets are correlated with their past positions. Additionally, we will know what kind of forces drive the motion of a droplet by looking at the slope of the dispersion relation. Since we also have data on what neighbours a droplet has at any time step, we can also define a relative dispersion, showing when a droplet is fully decorrelated from its neighbours. We expect droplets to be fully decorrelated around a time scale of $\tau = \frac{L}{v_{rms}}$, where L is the box size and v_{rms} is the root mean square velocity. This would be of the order of 10^5 time steps. Furthermore, we expect the slope to decrease after this decorrelation time, showing a transition from ballistic motion to dispersive motion, as is typical for the Brownian motion we expect droplets to move around with; examples can be found in the work of Calderó et al. [19] and De Anna et al. [20]. This will be expanded on in the discussion of the graphs below.

Starting with the absolute dispersion, it can be computed by taking the position difference between a droplet's position in time and its position at a given time step t_0 averaged over all droplets. The absolute dispersion is thus defined as

$$R_p(t) = \langle |x(t_0 + t) - x(t_0)|^2 \rangle, \tag{5.3}$$

where t_0 is the chosen initial time step and t determines the time step that is being compared with.

The relative dispersion instead compares a droplets position to the positions of its neighbours at the chosen time t_0 by taking the averaged position of their relative distances. It is given by

$$R_p(t - t_0; t_0) = \langle |x_j(t) - x_k(t)|^2 \rangle_{j,k,t_0}, \tag{5.4}$$

where j is the reference droplet and the droplets k are its neighbours at the initial time step t_0. This dispersion is expected to stay nearly constant for small t, as the neighbouring droplets k have a similar velocity to the droplet j for small time scales, meaning that they will stay close together for a short time. Following this, it is expected that the slope will change more slowly compared to the absolute dispersion after this initial period as well for the same reason.

The slope of the absolute dispersion indicates if a droplet is moving ballistically or diffusing. This can be seen in Fig. 5.7. By plotting this on a log-log scale, a slope of 2 is present for each volume fraction, corresponding to ballistic movement of the droplets at shorter times. In others
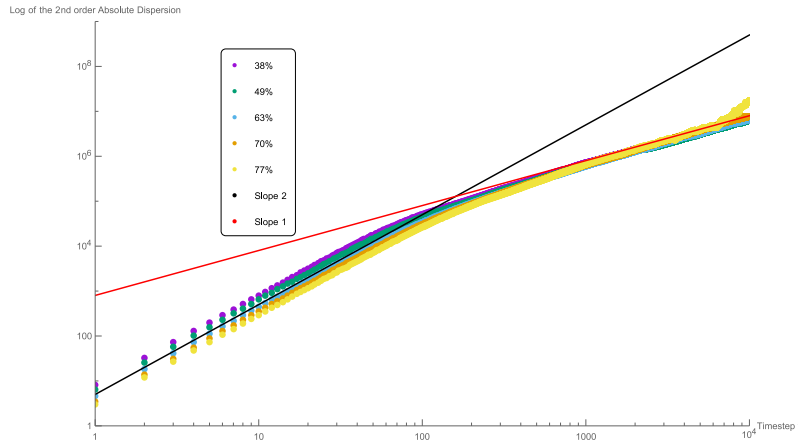

Figure 5.7: Absolute dispersion for different volume fractions.

Volume fraction	38%	49%	63%	70%	77%
Time scale $t_1 \cdot 10^3$	3.63	4.12	5.09	5.93	7.85
Time scale $t_2 \cdot 10^4$	7.45	8.82	10.4	11.0	12.5

Table 5.3: Table with the fit parameters resulting from applying Eq. 5.5 to the simulations with varying volume fraction.

words, the droplets initially move away from their initial position in a straight line. Mathematically, this slope of 2 comes from the order 2 of the dispersion that was used: rewriting Eq. 5.3 readily shows that a slope of 2 corresponds with the droplets moving as $x = v \cdot t$ on average. This ballistic motion continues until the slope reduces to 1 around $t \approx 10^3$, corresponding to diffusive motion, as diffusive motion is characterized by a dependence on $\sqrt{t}$. This means that this time scale corresponds to the time it takes for a droplet to be completely uncorrelated with its past trajectory. In other words, it takes an average of around 10^3 time steps for a droplet to have its trajectory influenced by interactions with other droplets to the point where its trajectory from then on is completely uncorrelated with the position it had at t_0.

While the above is also true for the relative dispersion, as can be seen in Fig. 5.8, a secondary time scale of order $O(t) = 10^2$ can be seen for the relative dispersion. This denotes the time it takes for a droplet j to decorrelate from the neighbouring droplets k. In order to estimate the two time scales, the following piecewise function was used:

$$R_{fit}(t) = \begin{cases} d\sqrt{1 + \frac{t^2}{t_1^2}} & t < t_2 \\ \frac{d}{t_1}\sqrt{t_2 t} & t \geq t_2 \end{cases} \tag{5.5}$$

This function was chosen because of a few characteristics that were expected to be relevant. The distance d is the relative dispersion at t_0, which is essentially the average droplet neighbour distance at that time. For small values of t, the relative dispersion can be approximated by d, hence the factor 1 under the square root in the first equation. For larger t, the first equation can be approximated by $R_{fit}(t) \approx \frac{d}{t_1} \cdot t$, corresponding to ballistic motion indicated by a linear dependence on t as with the absolute dispersion. Similarly, for $t \geq t_2$, the second equation of 5.5 corresponds to diffusive motion, indicated by the dependence on $\sqrt{t}$. The resulting values are given in Table ??.

Furthermore, it can be seen in Fig. 5.8 that the relative dispersion for low t is higher for high volume fractions. This is due to the fact that droplets are larger and fewer in number for high volume fractions (as can be seen in Fig. A.1). All the positions x in Eq. 5.4 are given as the centre of mass, causing the larger droplets to naturally have a larger dispersion for low t. As time increases past the aforementioned time scale, this relation reverses, with the lower volume fractions dispersing more quickly. In time, the larger droplets present at high volume fractions do not move away from their neighbours as quickly because of their size, as the lack of space to move around causes the droplets to stay close to their neighbours for longer. It should be noted that this happens to the bulk of the fluid: groups of droplets move as a whole with a certain velocity that is not much lower than the velocities seen for the lower volume fraction cases. This can be seen in Table 5.1.
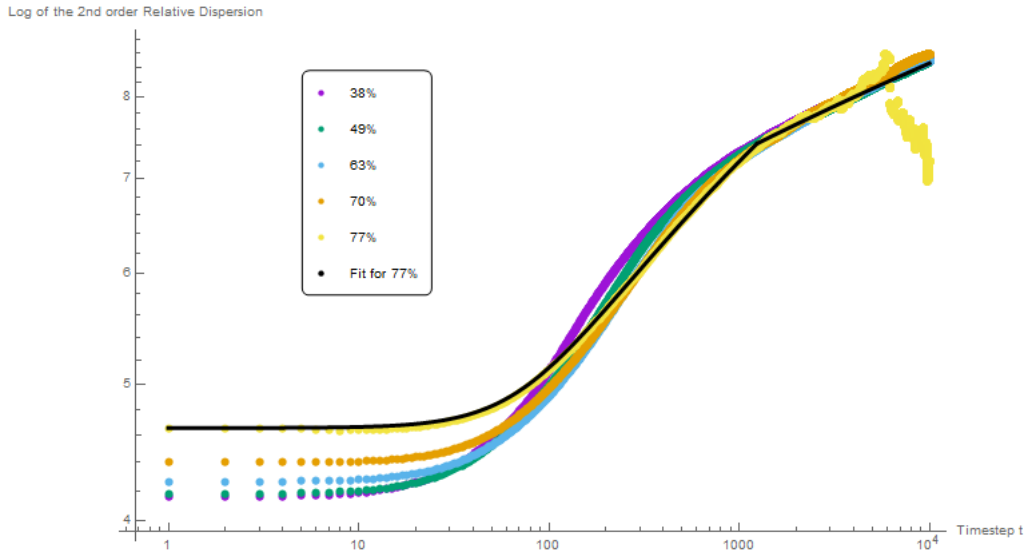
Figure 5.8: Relative dispersion for different volume fractions.

5.4 Lagrangian Structure Functions

As the droplets move around, their velocities change based on their interactions with their neighbours and, depending on the particular simulation, the applied stirring force.

Next to the dispersion in space, one can also analyse the correlation a Lagrangian particle, such as the droplets, have with themselves in terms of velocity. Taking the ensemble average for all droplets in time, we get the relation

$$S_2(\tau) = \langle |\boldsymbol{v}_k(t+\tau) - \boldsymbol{v}_k(t)|^2 \rangle_{k,t},\tag{5.6}$$

which is known as the Lagrangian structure function of order 2, where k is any droplet that exists at time t. Lagrangian structure functions are often used in the Lagrangian description of turbulence, see for example the work of Toschi Bodenschatz[21] and Benzi et al. [22]. While the system being studied here is not turbulent, the Lagrangian data we have makes for a good comparison to studies on Lagrangian turbulence. Kolmogorov theory on turbulence predicts that the slope of this quantity scales as a power law of r. In the inertial range, i.e. before diffusion becomes dominant, the slope of this quantity is expected be 1 [23].

Computing this for different volume fractions shows that the velocity is decorrelated after 10000-20000 time steps, though especially for lower volume fractions there is a distinguishable waveform on top of the constant value that is seen for high t. This is likely due to the aforementioned circular trajectories: because a significant amount of droplets move back to the same position after completing one cycle of this motion, their velocity naturally will also correlate more strongly with the velocity they had at the initial time t. Since droplets move around more freely for the lower volume fractions, there are less collisions and interactions with other droplets (see for example Figure 5.2), and hence the droplets will more readily follow the flow profile with their lower inertia. This could explain why the lower volume fractions show this waveform more strongly than higher volume fractions.

It should be noted that the statistics decrease for longer times t, as shown by the graph at the bottom-right of Fig. 5.9. In time, some droplets undergo breakup or coalescence events, which dramatically influences the velocities of the droplets, and hence they were not used for the statistics. This explains the high amount of noise for higher times t, as only a few dozen droplets were used for the statistics near the end of the graph. Note that this especially affects the higher
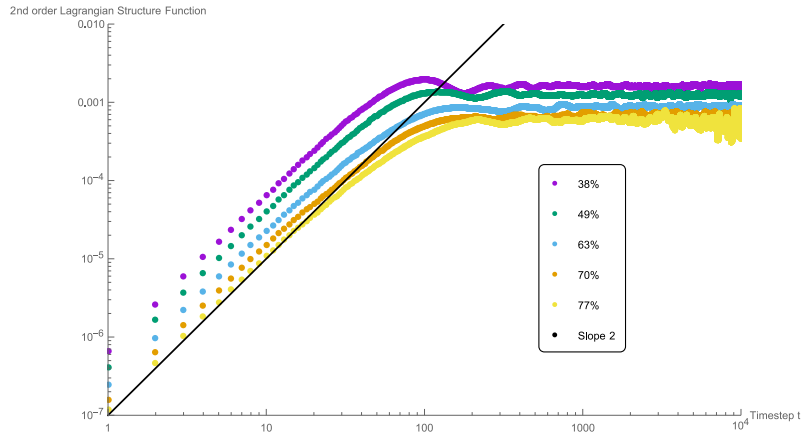
Figure 5.9: Second order velocity Lagrangian structure function for different volume fractions between 1-2 M time steps. In the bottom right, the amount of droplets used for this statistic is given, as in time, some droplets have breakup or coalescence events, making them unfit to be included in the statistics.

volume fractions, which undergo coalescence and breakup events much more frequently compared to the lower volume fraction cases.

5.5   Velocity gradient

In the work of Graner et al. [18], a framework of statistical tools for comparing two- or three-dimensional patterns is proposed. In this section, this framework is briefly explained and then applied to the Eulerian data we obtained, showing that the data is suitable for this type of analysis. The central ideas of this paper will be discussed, and we will show one of the derived quantities also shown in the paper, namely the velocity gradient.

The basis of this framework is to consider links, defined as a vector of the distances between the centre of mass a droplet and one of its neighbours, i.e.

$$\mathbf{l} = \mathbf{r}_1 - \mathbf{r}_2. \tag{5.7}$$

Droplets in binary emulsions are one example of the patterns than can be modelled this way: for our data, the positions $\mathbf{r}$ above are simply the centre of masses for two neighbouring droplets, i.e. $\mathbf{l}(X, Y, Z) = (x_1 - x_2, y_1 - y_2, z_1 - z_2)$. The framework has no other requirements or dependencies: it is independent of any stresses, masses or forces. Most of the statistics are then performed on the link matrix, defined as

$$M = \begin{pmatrix} \langle X^2 \rangle & \langle XY \rangle & \langle XZ \rangle \\ \langle XY \rangle & \langle Y^2 \rangle & \langle YZ \rangle \\ \langle XZ \rangle & \langle YZ \rangle & \langle Z^2 \rangle \end{pmatrix}, \tag{5.8}$$

where the averages denoted by the brackets $\langle \rangle$ are taken over all of a droplet's neighbours. This definition for M contains information on the relative position but also the square length by taking its trace and, for consecutive time steps, changes in angle. After introducing this quantity M, the paper then follows by introducing a number of quantities which are computed through through ensemble averages of this link matrix, one for each droplet.

The description given by M is still discrete, as it depends on the locations of the droplets. In order to give a continuous description, the statistical velocity gradient W has a dimension of a strain rate (s^{-1}). This velocity gradient is continuous and independent of the droplets themselves.

It is given by

$$W = \langle l \otimes l \rangle^{-1} \langle l \otimes \frac{dl}{dt} \rangle. \tag{5.9}$$

It is given here for completeness; a thorough overview of why this function describes a velocity gradient is given in appendix C of the work of Graner et al. [18].

This gradient vector field can be used to study systems like the ones in this thesis. The results are included here to show that the framework as presented in the paper can be applied with the LBE3D simulations on binary emulsions, similar to an example study from the same authors [24]. This can be done because the framework does not rely on the morphology of the droplets, which is important as the data we have only lists the position of the centre of mass. The details of the method can be found in these two papers [18] [24].

An example is given in Fig. 5.10, which shows the velocity gradients of each droplet. These are calculated by taking the eigenvalues and their corresponding eigenvectors of the symmetric part of the matrix W. These are then visualized as ellipsoids with the longest bases pointing in the direction of the strongest gradient. Much like could be inferred from the trajectories seen in section 5.1, these gradient suggest a clear anisotropy in the velocity gradients.

This framework can be applied for studying dense binary emulsions, and could be expanded on in the future in order to, for instance, give information on the viscosity and the strain rates present in the system, as was done in the original paper assuming a steady system.
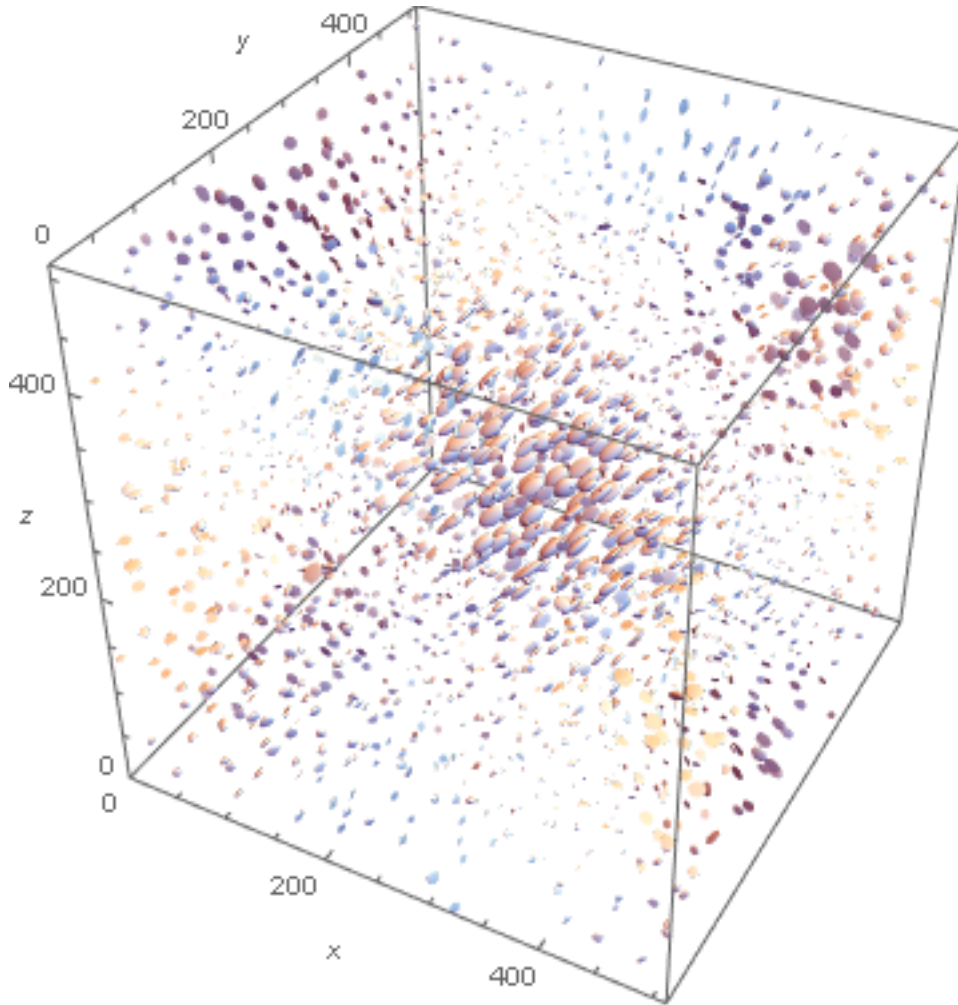
Figure 5.10: Velocity gradient for the 60% volume fraction case, made using the velocity gradient W as defined by links from [18]. The ellipsoids represent the velocity gradients of each droplet at time step 2800000. The longest base of the ellipsoids represent the direction in which the velocity gradient is the largest. Note that in order to visualise this, the symmetrical part of W was used, i.e. $\frac{W+W^t}{2}$

.

5.6 Summary

This chapter gave the results of a preliminary analysis done using the tracking algorithm. We discussed the trajectories and the PDFs of the velocity and acceleration. From this, an isotropy in the velocities of the droplets was noted, likely caused by an error in parametrization of the stirring force. The dispersion showed the predicted behaviour, transitioning to a diffusive regime for later time steps. The relative dispersion took longer to decorrelate compared to the absolute dispersion, giving two different time scales. The Lagrangian structure functions were comparable to the absolute dispersion, save for a noticeable periodic structure which was attributed to the vortex-like motions that can be seen in the trajectories. Finally, we looked at a framework from a paper to show it can be used to analyse dense emulsions with the methodology described in this thesis, and compared a continuous velocity gradient we obtained from it with a velocity gradient that was interpolated directly from the data.

Chapter 6

Conclusions

In this thesis, we studied the flow of dense emulsions through fully developed numerical simulations made with the LBE3D code. We did this by developing a tracking algorithm that allows us to study the statistics of the dispersed phase. We also used the obtained data to look at the trajectories of individual droplets, derive statistics in the form of PDFs and dispersion graphs, and applying the data to the framework of the work of Graner et al. [18].

We were able to accurately track the droplets, which cannot be done at this scale experimentally. Additionally, we can know how often the tracking fails due to droplets being marked prior to the tracking itself, which showed a low error rate that is negligible for all but the largest volume fraction case. The data obtained through the tracking is flexible by being available in both Lagrangian and Eulerian formats, which aids in the ease of analysing the large amounts of data that were used.

During the analysis, it was noted that the stirring force was not anisotropic as it was intended, causing patterns to occur in the trajectories and the other statistics. This did not, however, significantly impact the dispersion and the Lagrangian structure functions, which did show the expected behaviour of transitioning from a ballistic regime to a diffusive one.

One unexpected result did occur for the high volume fraction cases, as which the PDFs fit well to a triple Gaussian. Two explanations for this were given, one being a possible caging effect, in which a droplet can achieve a high velocity if it gets stuck between surrounding droplets moving in on it from different directions. The other explanation lies in the aforementioned fault in the stirring force, which could have an impact the statistics.

Finally, the framework given in the work of Graner et al. [18] was successfully implemented, and a novel way of visualising the velocity gradient was given.

Bibliography

[1] David Julian Mcclements. Critical review of techniques and methodologies for characterization of emulsion stability. *Critical reviews in food science and nutrition*, 47(7):611–649, 2007. 1

[2] JH Abou-Kassem and SM Ali. Modeling of emulsion flow in porous media. *Journal of Canadian Petroleum Technology*, 34(06), 1995. 1

[3] Lijuan Wang, Xuefeng Li, Gaoyong Zhang, Jinfeng Dong, and Julian Eastoe. Oil-in-water nanoemulsions for pesticide formulations. *Journal of colloid and interface science*, 314(1):230–235, 2007. 1

[4] Ivan Girotto. Physics of dense emulsions via high-performance fully resolved simulations. 2021. 1, 2, 10, 11

[5] Ivan Girotto, Karun Datadien, Gianluca Di Staso, and Federico Toschi. Video: The chaotic life of mayonnaise. In *72th Annual Meeting of the APS Division of Fluid Dynamics - Gallery of Fluid Motion*. American Physical Society, November 2019. 2

[6] S Yanniotis, S Skaltsi, and S Karaburnioti. Effect of moisture content on the viscosity of honey at different temperatures. *Journal of Food Engineering*, 72(4):372–377, 2006. 3

[7] JF Swindells, JR Coe Jr, and TB Godfrey. Absolute viscosity of water at 20 c. *Journal of Research of the National Bureau of Standard*, 48(1), 1952. 3

[8] James Welty, Gregory L Rorrer, and David G Foster. *Fundamentals of momentum, heat, and mass transfer*. John Wiley & Sons, 2014. 4

[9] Frans TM Nieuwstadt, Jerry Westerweel, and Bendiks J Boersma. *Turbulence: introduction to theory and applications of turbulent flows*. Springer, 2016. 6

[10] P. L. Bhatnagar, E. P. Gross, and M. Krook. A Model for Collision Processes in Gases. I. Small Amplitude Processes in Charged and Neutral One-Component Systems. *Physical Review*, 94(3):511–525, May 1954. 10

[11] Shiyi Chen and Gary D Doolen. Lattice boltzmann method for fluid flows. *Annual review of fluid mechanics*, 30(1):329–364, 1998. 10

[12] Ivan Girotto, Sebastiano Fabio Schifano, Enrico Calore, Gianluca Di Staso, and Federico Toschi. Performance and energy assessment of a lattice boltzmann method based application on the skylake processor. *Computation*, 8(2), 2020. 10

[13] Massimo Bernaschi, Massimiliano Fatica, Simone Melchionna, Sauro Succi, and Efthimios Kaxiras. A flexible high-performance lattice boltzmann gpu code for the simulations of fluid flows in complex geometries. *Concurrency and computation: practice and experience*, 22(1):1–14, 2010. 10

[14] M Sbragaglia, R Benzi, M Bernaschi, and S Succi. The emergence of supramolecular forces from lattice kinetic models of non-ideal fluids: applications to the rheology of soft glassy materials. *Soft Matter*, 8(41):10773–10782, 2012. 10

[15] Xiaowen Shan and Hudong Chen. Lattice boltzmann model for simulating flows with multiple phases and components. *Physical review E*, 47(3):1815, 1993. 11

[16] Roberto Benzi, Mauro Sbragaglia, Sauro Succi, Massimo Bernaschi, and Sergio Chibbaro. Mesoscopic lattice boltzmann modeling of soft-glassy systems: theory and simulations. *The Journal of Chemical Physics*, 131(10):104903, 2009. 11

[17] R Benzi, M Sbragaglia, P Perlekar, M Bernaschi, S Succi, and F Toschi. Direct evidence of plastic events and dynamic heterogeneities in soft-glasses. *Soft Matter*, 10(26):4615–4624, 2014. 11

[18] François Graner, Benjamin Dollet, Christophe Raufaste, and Philippe Marmottant. Discrete rearranging disordered patterns, part i: Robust statistical tools in two or three dimensions. *The European Physical Journal E*, 25(4):349–369, 2008. 21, 30, 31, 32, 35

[19] Gabriela Calderó, Alessandro Patti, Meritxell Llinàs, and Maria José García-Celma. Diffusion in highly concentrated emulsions. *Current opinion in colloid & interface science*, 17(5):255–260, 2012. 27

[20] Pietro De Anna, Tanguy Le Borgne, Marco Dentz, Alexandre M Tartakovsky, Diogo Bolster, and Philippe Davy. Flow intermittency, dispersion, and correlated continuous time random walks in porous media. *Physical review letters*, 110(18):184502, 2013. 27

[21] Federico Toschi and Eberhard Bodenschatz. Lagrangian properties of particles in turbulence. *Annual review of fluid mechanics*, 41:375–404, 2009. 29

[22] R Benzi, S Ciliberto, Raffaele Tripiccione, C Baudet, F Massaioli, and S Succi. Extended self-similarity in turbulent flows. *Physical review E*, 48(1):R29, 1993. 29

[23] Andrei Sergeevich Monin and AM Yaglom. Statistical fluid mechanics ii, 1975. 29

[24] Philippe Marmottant, Christophe Raufaste, and François Graner. Discrete rearranging disordered patterns, part ii: 2d plasticity, elasticity and flow of a foam. *The European Physical Journal E*, 25(4):371–384, 2008. 31
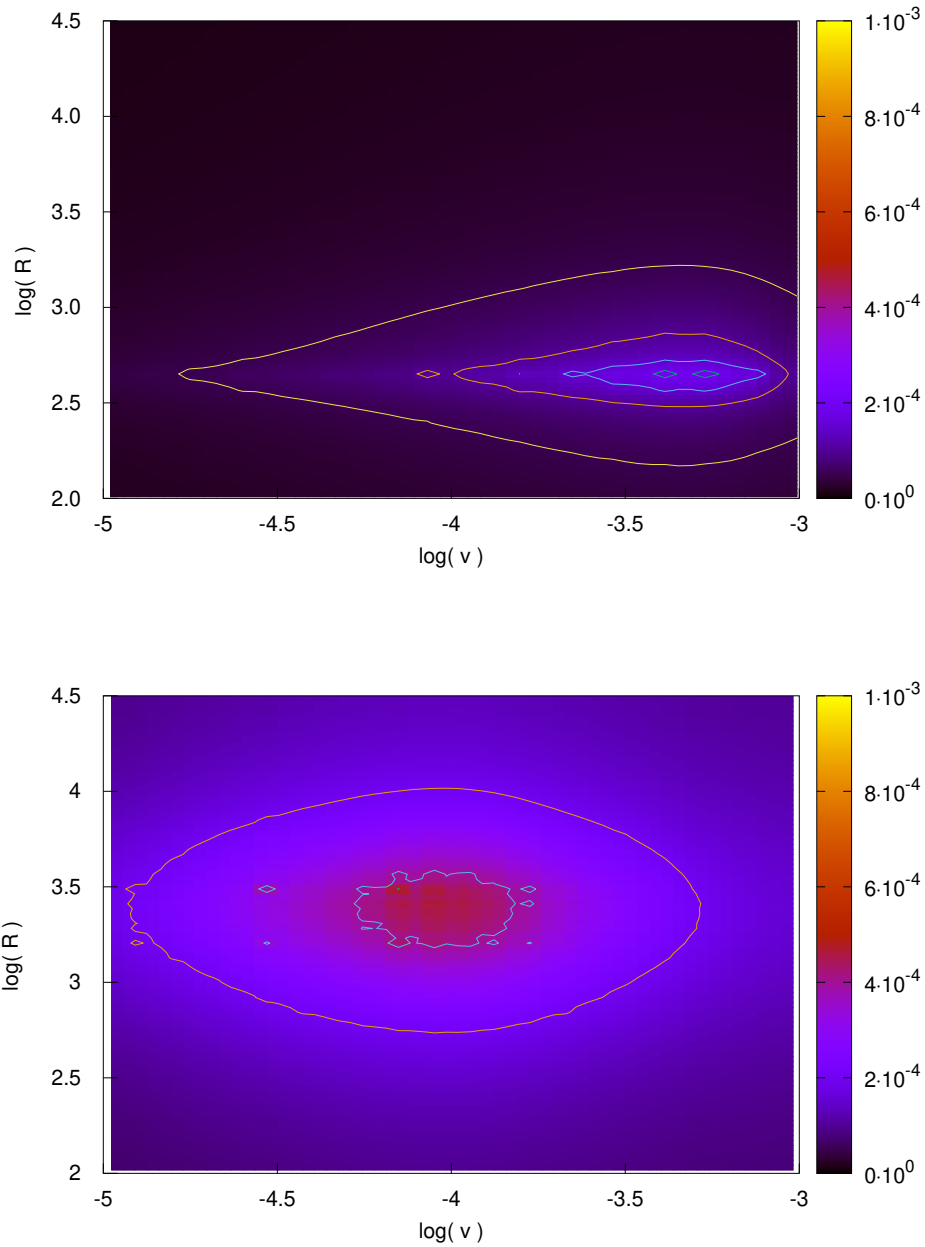
Appendix A

Appendix

Figure A.1: 2D histogram of the radius of droplets for varying velocities. The velocities are given in terms of v_{rms}. The top image was done for a low volume fraction of 38%, whereas the bottom image was done for a high volume fraction of 77%, both over a period of $2 \cdot 10^6$ time steps.